

## Iron-corrected Single-epoch Black Hole Masses of DESI Quasars at low redshift

ZHIWEI PAN,<sup>1,2</sup> LINHUA JIANG,<sup>1,2</sup> WEI-JIAN GUO,<sup>3</sup> SHENGXIU SUN,<sup>1,2</sup> MALGORZATA SIUDEK,<sup>4</sup> JESSICA NICOLE AGUILAR,<sup>5</sup>  
STEVEN AHLEN,<sup>6</sup> DAVID BROOKS,<sup>7</sup> TODD CLAYBAUGH,<sup>5</sup> AXEL DE LA MACORRA,<sup>8</sup> PETER DOEL,<sup>7</sup>  
ENRIQUE GAZTAÑAGA,<sup>9,10,4</sup> SATYA GONTCHO A GONTCHO,<sup>5</sup> STEPHANIE JUNEAU,<sup>11</sup> THEODORE KISNER,<sup>5</sup>  
ANDREW LAMBERT,<sup>5</sup> MARTIN LANDRIAU,<sup>5</sup> LAURENT LE GUILLOU,<sup>12</sup> MARC MANERA,<sup>13,14</sup> PAUL MARTINI,<sup>15,16,17</sup>  
AARON MEISNER,<sup>11</sup> RAMON MIQUEL,<sup>18,14</sup> JOHN MOUSTAKAS,<sup>19</sup> ADAM MYERS,<sup>20</sup> CLAIRE POPPETT,<sup>5,21,22</sup>  
FRANCISCO PRADA,<sup>23</sup> GRAZIANO ROSSI,<sup>24</sup> EUSEBIO SANCHEZ,<sup>25</sup> MICHAEL SCHUBNEL,<sup>26,27</sup> HEE-JONG SEO,<sup>28</sup>  
DAVID SPRAYBERRY,<sup>11</sup> GREGORY TARLÉ,<sup>27</sup> BENJAMIN ALAN WEAVER,<sup>11</sup> AND HU ZOU<sup>29</sup>

<sup>1</sup>*Department of Astronomy, School of Physics, Peking University, Beijing 100871, China*

<sup>2</sup>*Kaoli Institute for Astronomy and Astrophysics, Peking University, Beijing 100871, China*

<sup>3</sup>*Key Laboratory of Optical Astronomy, National Astronomical Observatories, Chinese Academy of Sciences, Beijing 100012, China*

<sup>4</sup>*Institute of Space Sciences, ICE-CSIC, Campus UAB, Carrer de Can Magrans s/n, 08913 Bellaterra, Barcelona, Spain*

<sup>5</sup>*Lawrence Berkeley National Laboratory, 1 Cyclotron Road, Berkeley, CA 94720, USA*

<sup>6</sup>*Physics Dept., Boston University, 590 Commonwealth Avenue, Boston, MA 02215, USA*

<sup>7</sup>*Department of Physics & Astronomy, University College London, Gower Street, London, WC1E 6BT, UK*

<sup>8</sup>*Instituto de Física, Universidad Nacional Autónoma de México, Cd. de México C.P. 04510, México*

<sup>9</sup>*Institut d'Estudis Espacials de Catalunya (IEEC), 08034 Barcelona, Spain*

<sup>10</sup>*Institute of Cosmology and Gravitation, University of Portsmouth, Dennis Sciama Building, Portsmouth, PO1 3FX, UK*

<sup>11</sup>*NSF NOIRLab, 950 N. Cherry Ave., Tucson, AZ 85719, USA*

<sup>12</sup>*Sorbonne Université, CNRS/IN2P3, Laboratoire de Physique Nucléaire et de Hautes Energies (LPNHE), FR-75005 Paris, France*

<sup>13</sup>*Departament de Física, Serra Hünter, Universitat Autònoma de Barcelona, 08193 Bellaterra (Barcelona), Spain*

<sup>14</sup>*Institut de Física d'Altes Energies (IFAE), The Barcelona Institute of Science and Technology, Campus UAB, 08193 Bellaterra Barcelona, Spain*

<sup>15</sup>*Center for Cosmology and AstroParticle Physics, The Ohio State University, 191 West Woodruff Avenue, Columbus, OH 43210, USA*

<sup>16</sup>*Department of Astronomy, The Ohio State University, 4055 McPherson Laboratory, 140 W 18th Avenue, Columbus, OH 43210, USA*

<sup>17</sup>*The Ohio State University, Columbus, 43210 OH, USA*

<sup>18</sup>*Institució Catalana de Recerca i Estudis Avançats, Passeig de Lluís Companys, 23, 08010 Barcelona, Spain*

<sup>19</sup>*Department of Physics and Astronomy, Siena College, 515 Loudon Road, Loudonville, NY 12211, USA*

<sup>20</sup>*Department of Physics & Astronomy, University of Wyoming, 1000 E. University, Dept. 3905, Laramie, WY 82071, USA*

<sup>21</sup>*Space Sciences Laboratory, University of California, Berkeley, 7 Gauss Way, Berkeley, CA 94720, USA*

<sup>22</sup>*University of California, Berkeley, 110 Sproul Hall #5800 Berkeley, CA 94720, USA*

<sup>23</sup>*Instituto de Astrofísica de Andalucía (CSIC), Glorieta de la Astronomía, s/n, E-18008 Granada, Spain*

<sup>24</sup>*Department of Physics and Astronomy, Sejong University, Seoul, 143-747, Korea*

<sup>25</sup>*CIEMAT, Avenida Complutense 40, E-28040 Madrid, Spain*

<sup>26</sup>*Department of Physics, University of Michigan, Ann Arbor, MI 48109, USA*

<sup>27</sup>*University of Michigan, Ann Arbor, MI 48109, USA*

<sup>28</sup>*Department of Physics & Astronomy, Ohio University, Athens, OH 45701, USA*

<sup>29</sup>*National Astronomical Observatories, Chinese Academy of Sciences, A20 Datun Rd., Chaoyang District, Beijing, 100012, P.R. China*

## ABSTRACT

We present a study on the possible overestimation of single-epoch supermassive black hole (SMBH) masses in previous works, based on more than 55,000 type 1 quasars at  $0.25 < z < 0.8$  from the Dark Energy Spectroscopic Instrument (DESI). We confirm that iron emission strength serves as a good tracer of the Eddington ratio, and estimate SMBH masses using an iron-corrected  $R$ - $L$  relation for  $H\beta$ , where  $R$  is the broad line region size and  $L$  is the continuum luminosity. Compared to our measurements, previous canonical measurements without the iron correction are overestimated by a factor of 1.5 on average. The overestimation can be up to a factor of 5 for super-Eddington quasars. The fraction of super-Eddington quasars in our sample is about 5%, significantly higher than 0.4% derived from the canonical measurements. Using a sample featuring both  $H\beta$  and Mg II emission lines, we calibrate Mg II-based SMBH masses using iron-corrected,  $H\beta$ -based SMBH masses and establish an iron-corrected  $R$ - $L$  relation for Mg II. The new relation adds an extra term of  $-0.34R_{\text{Fe}}$  to the  $R$ - $L$

relation, where  $R_{\text{Fe}}$  denotes the relative iron strength. We use this formula to build a catalog of about 0.5 million DESI quasars at  $0.6 < z < 1.6$ . If these iron-corrected  $R$ - $L$  relations for  $\text{H}\beta$  and  $\text{Mg II}$  are valid at high redshift, current mass measurements of luminous quasars at  $z \geq 6$  would have been overestimated by a factor of 2.3 on average, alleviating the tension between SMBH mass and growth history in the early universe.

*Keywords:* Active galactic nuclei (16); Quasars (1319); Supermassive black holes (1663)

## 1. INTRODUCTION

Quasars are generally accepted to be powered by the gravitational potential energy extracted from matter falling toward supermassive black holes (SMBHs). The study of quasar luminosity function and black hole mass function over cosmic time has enriched our understanding of physical processes related to the growth history of SMBHs (Richards et al. 2006; Kelly & Shen 2013; Shen et al. 2020; Pan et al. 2022; Wu et al. 2022; Yang et al. 2023; Li et al. 2023; Fan et al. 2023). Reliable SMBH mass measurements are of fundamental importance in determining the properties of quasars and SMBHs. Strong and broad emission lines originating from broad line regions (BLRs), including  $\text{H}\alpha$ ,  $\text{H}\beta$ ,  $\text{Mg II}$ , and  $\text{C IV}$ , are frequently used to measure SMBH masses. Usually, we assume that the BLR gas moves virially under gravity (Peterson & Wandel 1999), then the central SMBH mass can be estimated by the BLR size  $R_{\text{BLR}}$  and the velocity width  $\Delta V$ :

$$M = f \frac{R_{\text{BLR}} \Delta V^2}{G}, \quad (1)$$

where  $f$  is the virial factor related to the geometry and kinematics of the BLR, and  $G$  is the gravitational constant. Reverberation mapping (RM) measures  $R_{\text{BLR}}$  via a time lag between the continuum and line flux (see Peterson 1993 and Cackett et al. 2021 for reviews). The emission-line profile of quasar spectra is used to measure  $\Delta V$ , which has been widely represented by the full width at half-maximum (FWHM) and the line dispersion  $\sigma_{\text{line}}$ .

Although SMBH masses estimated from RM are usually robust, such a technique requires rich observational resources. Astronomers have tried to develop easier methods (e.g., Vestergaard 2002) in the past few decades. For example, we can use single-epoch spectra to replace multi-epoch spectra, and thus use the empirical relation between the BLR size and the continuum luminosity (hereafter  $R$ - $L$  relation) to replace the time lag when estimating  $R_{\text{BLR}}$ . This type of scaling relations is not as robust as RM, so the RM results have been used to calibrate single-epoch scaling relations. Among these relations, the  $R_{\text{BLR}}(\text{H}\beta)$ - $L_{5100}$  relation is the most reliable one, where  $L_{5100}$  is the monochromatic luminosity

( $\lambda L_{\lambda}$ ) at 5100 Å, since the Balmer lines  $\text{H}\alpha$  and  $\text{H}\beta$  in the rest-frame optical range are the basis for the majority of low-redshift RM programmes (e.g., Kaspi et al. 2000; Bentz et al. 2006, 2013; Grier et al. 2017; Wang et al. 2020; Ma et al. 2023; Cho et al. 2023).  $\text{H}\alpha$  has been served as a substitute when  $\text{H}\beta$  is unavailable (e.g., Greene & Ho 2005; Grier et al. 2017; Cho et al. 2023). It is less popular than  $\text{H}\beta$  because it presents more observational challenges and its applicability is limited to a narrower redshift range.

In the rest-frame UV wavelength range, researchers have extended this approach to consider other emission lines such as  $\text{Mg II}$  and  $\text{C IV}$  (Vestergaard 2002; Warner et al. 2004; Vestergaard & Osmer 2009; Le et al. 2020; Shen et al. 2024). The scaling relations based on  $\text{Mg II}$  and  $\text{C IV}$  play a crucial role in estimating the SMBH masses of higher-redshift ( $z > 1$ ) Active Galactic Nuclei (AGNs) because  $\text{H}\beta$  moves out of the observed-frame optical range. Several RM studies have been conducted to investigate the  $R$ - $L$  relations using  $\text{Mg II}$  and  $\text{C IV}$  (e.g., Metzroth et al. 2006; Kaspi et al. 2007; Lira et al. 2018; Hoormann et al. 2019; Yu et al. 2021, 2023; Shen et al. 2024). These relations are not as tight as those from  $\text{H}\beta$  or  $\text{H}\alpha$ . Consequently, UV mass estimators require calibration against  $\text{H}\beta$ -based measurements, including time lags (representing the BLR size) and mass estimates (e.g., Woo et al. 2018; Le et al. 2020). While the calibrated relations generally align, the scatter of the  $\text{C IV}$ -based relation is significantly larger than those of the  $\text{Mg II}$ -based and  $\text{H}\beta$ -based relations (e.g., Trakhtenbrot & Netzer 2012; Coatman et al. 2017).

In the past several years, there is accumulating evidence suggesting an increasing scatter in the  $R$ - $L$  relation (e.g., Shen et al. 2024). Astronomers have identified some reasons, including accretion states that can influence the canonical  $R$ - $L$  relation (Wang et al. 2014a,b; McHardy et al. 2018; GRAVITY Collaboration et al. 2024). In particular, the Super-Eddington Accreting Massive Black Hole (SEAMBH) campaign has uncovered that many AGNs with strong  $\text{Fe II}$  and narrow  $\text{H}\beta$  emission lines, possibly indicating high accretion rates, deviate from the traditional  $R$ - $L$  relation (Du et al. 2015, 2018). The study by Du & Wang (2019) claimed

that the flux ratio between the Fe II and H $\beta$  lines is strongly correlated with the deviation from the  $R$ - $L$  relation. Furthermore, Woo et al. (2024) observed that most of their AGNs fall below the canonical relation, with the deviation potentially linked to the Eddington ratio. They identified a tentative correlation involving the relative Fe II strength. Spectro-interferometric results by GRAVITY Collaboration et al. (2024) and Abuter et al. (2024) also appear to support the hypothesis that the Eddington ratio is indeed a factor influencing the  $R$ - $L$  relation.

In terms of theory, many assumptions underlie the canonical  $R$ - $L$  relation, including the isotropic assumptions, proportional assumptions, point source assumptions (Du & Wang 2019). These conditions are tailored to the standard disk model with a normal accretion rate, suggesting that dependences of the  $R$ - $L$  relation extend to the accretion state and even other properties. Consequently, the extended  $R$ - $L$  relation is proposed to incorporate the Fe II strength, aiming to provide less biased single-epoch estimations of the H $\beta$ -based SMBH mass and accretion rate (Du & Wang 2019; Yu et al. 2020).

The necessity for an iron correction in the Mg II-based SMBH mass estimations remains uncertain. Dong et al. (2011) observed a strong correlation between the Eddington ratio and the intensity ratios of both ultraviolet and optical Fe II emission to Mg II. In a related context, Martínez-Aldama et al. (2020) suggested that a smaller scatter can be achieved through a linear combination of  $L_{5100}$  and the strength of UV Fe II. Conversely, some studies claimed that current Mg II samples consistently adhere to the canonical 2-parameter  $R$ - $L$  relation (Khadka et al. 2022; Yu et al. 2023). Further validation is crucial with a need for a more extensive and well-defined RM-calibrated sample in the future.

In this paper, we adopt the iron-corrected  $R$ - $L$  relation proposed by Du & Wang (2019). Then we utilize the corrected H $\beta$ -based SMBH mass as a reference to calibrate the Mg II-based SMBH mass. Despite the absence of new RM results, we leverage the high spectral resolution, high data quality, and large sample size of the Dark Energy Spectroscopic Instrument (DESI) to investigate DESI SMBH mass estimation with iron correction. We will not distinguish between AGNs and quasars in the following since we focus on the luminous sources. We use FWHM to represent the velocity width  $\Delta V$ . The layout of the paper is as follows. In Section 2, we outline the data from DESI, detailing fitting procedures and spectral measurements. Section 3 presents our quasar sample and corresponding analyses. In Section 4, we assess the robustness of our conclusions, make comparisons between different SMBH mass estimators,

and discuss the implications. We summarize the paper in Section 5. Throughout this paper, magnitudes are expressed in the AB system. We adopt a  $\Lambda$ -dominated flat cosmology with  $H_0 = 70 \text{ km s}^{-1} \text{ Mpc}^{-1}$ ,  $\Omega_m = 0.3$ , and  $\Omega_\Lambda = 0.7$ .

## 2. DATA AND MEASUREMENTS

This section offers a concise overview of the DESI imaging survey and DESI spectroscopic survey. Furthermore, we illustrate the steps involved in creating the parent sample and performing spectral fitting for this sample.

### 2.1. DESI

DESI, a Stage IV ground-based dark energy experiment, utilizes the 4 m Mayall telescope at Kitt Peak National Observatory to investigate the expansion history via baryon acoustic oscillations and cosmic structure growth through redshift-space distortions (DESI Collaboration et al. 2016a,b, 2022, 2024a,b,c). Equipped with 5,000 fibers on the focal plane, DESI is conducting the largest multiobject spectral survey, efficiently observing approximately 40 million galaxies and quasars across 14,000 square degrees during its 5-year mission (DESI Collaboration et al. 2016a,b; Silber et al. 2023; Miller et al. 2023). It reaches a limiting magnitude of about 23 mag in the  $r$  band, enabling the discovery of faint and high-redshift quasars (Chaussidon et al. 2023). Furthermore, DESI has good spectral resolutions in its three optical channels (blue: 3600–5900 Å, green: 5660–7220 Å, and red: 7470–9800 Å) with respective resolutions of approximately  $R \sim 2700$ ,  $R \sim 4200$ , and  $R \sim 4600$  (DESI Collaboration et al. 2022).

Before starting the Main Survey, DESI launched a 5-month Survey Validation (SV) campaign in December 2020. The SV campaign consisted of three phases intending to validate the selection of the targets, the development of the operations (Schlafly et al. 2023), and the further optimization over an area equal to 1% of the Main Survey (DESI Collaboration et al. 2024d). The entire SV data is publicly released as the DESI Early Data Release (DESI Collaboration et al. 2024e). Detailed information about the selection and validation for quasars, bright galaxies, emission-line galaxies, and luminous red galaxies from the SV data can be found in recent DESI publications (e.g., Yèche et al. 2020; Chaussidon et al. 2023; Raichoor et al. 2023; Yang et al. 2023; Zhou et al. 2023; Lan et al. 2023). Furthermore, comprehensive insights into the pipelines designed for DESI target selections and spectral reduction are presented in Myers et al. (2023) and Guy et al. (2023), respectively.

DESI employed a combination of three methods for quasar classification during SV: Redrock, a template-

fitting classifier (Bailey et al. in preparation); Mg II Afterburner, a broad Mg II line finder (Chaussidon et al. 2023); and QuasarNET, a deep convolutional neural network classifier (Busca & Balland 2018; Farr et al. 2020). Subsequently, visual inspection was implemented to assess spectroscopic quality and redshift reliability, which reduced misclassified quasars and enhanced the performance of standard pipelines (Alexander et al. 2023).

The spectra used in this work were obtained from the internal dataset called Iron, which is processed by the DESI pipeline. The Iron dataset that includes data from the SV and Year 1 phase will be published as part of the DESI Data Release 1 (DR1; DESI Collaboration et al. in preparation). To ensure that the spectral type classified by the pipeline is a quasar with a reliable redshift, we specifically selected those with SPECTYPE == “qso” and ZWARN == 0.

## 2.2. DESI Legacy Imaging Survey

The target selection of DESI relies on the imaging data from the DESI Legacy Surveys (Zou et al. 2017; Dey et al. 2019). The DESI Legacy Imaging Survey covers about 14,000 square degrees of the sky, with 9900 square degrees in the North Galactic Cap and 4400 square degrees in the South Galactic Cap regions. It was comprised of three distinct projects: the Dark Energy Camera Legacy Survey (DECaLS; Dey et al. 2019), the Beijing-Arizona Sky Survey (BASS; Zou et al. 2017), and the Mayall z-band Legacy Survey (MzLS; Dey et al. 2019). This imaging survey employed three bands and achieved approximate AB magnitudes of  $g = 24.0$ ,  $r = 23.4$ , and  $z = 22.5$  (Dey et al. 2019). The photometric magnitudes from the Legacy Survey were utilized in this work.

## 2.3. Parent Sample

The “Iron” dataset, spanning from December 14th, 2020, to June 13th, 2022, contains approximately 1.4 million quasar spectra. In this preliminary study, our primary focus is on high-quality, bright quasars, so we used the following selection criteria:  $0.25 < z < 0.8$ ,  $r < 20.5$  mag, and  $\text{TSNR}_{\text{QSO}} > 25$ , where  $\text{TSNR}_{\text{QSO}}$  is the template signal-to-noise ratio (S/N) for quasar class (Guy et al. 2023). The redshift cuts of 0.25 and 0.8 are constrained by the presence of Mg II and H $\beta$ , respectively. We selected bright quasars to minimize the influence from the host galaxy. As a result, we collected a total of 55,192 quasars as our parent sample. We then performed data preprocessing that includes correcting the spectra for galactic extinction and shifting the spectra to the rest frame. We adopted the galactic extinction curve proposed by Fitzpatrick (1999) with an assumed value of  $R_V = 3.1$ .

## 2.4. Spectral Fitting

DASpec<sup>1</sup> is a versatile multi-component spectral fitting tool designed for AGNs, featuring a user-friendly graphical interface. It uses the popular Levenberg-Marquardt algorithm and the Simulated Annealing algorithm for the least squares fitting of the curves. Because this software offers the capability to tie or fix parameters during the fitting process, we utilized DASpec to perform individual spectral fitting within the optical and UV spectral regions for our parent sample.

In the optical spectral region, our analysis comprises the following components: (1) a power-law continuum, (2) an Fe II pseudo-continuum template developed by Boroson & Green (1992), (3) two Gaussian profiles to characterize the broad H $\beta$  component, (4) individual Gaussian profiles for narrow emission lines, such as [O III]  $\lambda\lambda 4959, 5007$  and the narrow H $\beta$  component, and (5) a single Gaussian profile to model the broad He II line. Notably, all narrow-line components for each object share the identical velocity width and shift. Additionally, [O III]  $\lambda 4959$  is constrained to have one-third of the [O III]  $\lambda 5007$  flux, following the prescription from Osterbrock & Ferland (2006). The fitting procedure is executed within specific wavelength windows in the rest frame, spanning 3750–4000 Å, 4170–4260 Å, and 4430–5500 Å. The example of multicomponent spectral fitting in the optical region is illustrated in Figure 1.

In the UV spectral region, our analysis comprises the following components: (1) a power-law continuum, (2) an Fe II pseudo-continuum template developed by Tsuzuki et al. (2006, hereafter T06 template), (3) two Gaussian profiles to characterize the broad Mg II component, (4) a single Gaussian profile to characterize the narrow Mg II component, (5) the Balmer continuum and high-order Balmer lines, following Hu et al. (2008). The fitting procedure is executed within specific wavelength windows in the rest frame, spanning 2200–3500 Å, 3625–3645 Å, and 4170–4260 Å. The window 3625–3645 Å is utilized to impose constraints on the Balmer continuum emission due to the absence of pronounced Fe emission here (Wills et al. 1985). It is difficult to obtain a robust narrow Mg II component and a Balmer continuum, but their influence on the final results is negligible. The example of multicomponent spectral fitting in the UV region is illustrated in Figure 2.

Throughout our study, we set the boundary between narrow and broad lines at 1200 km s<sup>-1</sup> (Shen et al. 2011). The Fe II template was convolved with a Gaussian profile that can be scaled, broadened, and

<sup>1</sup> <https://github.com/PuDu-Astro/DASpec>



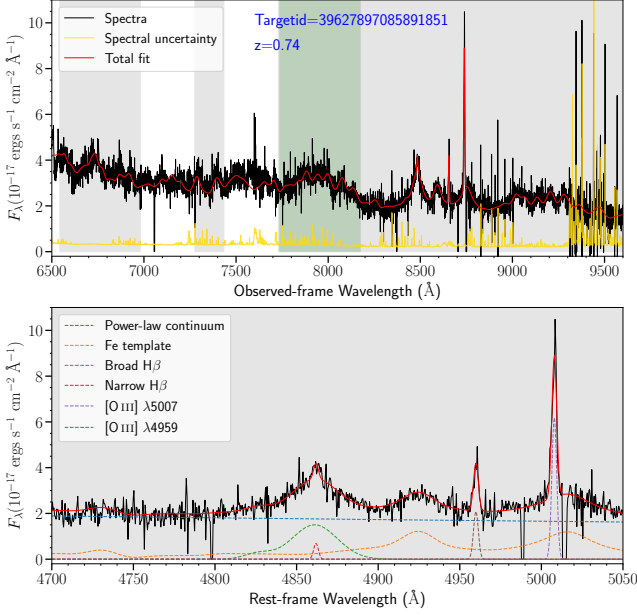


**Figure 1.** A fitting with strong iron strength in the rest-frame optical region. In the upper panel, the black solid line represents the observed-frame spectrum following correction for galactic extinction, and the yellow solid line represents the spectral uncertainty. The red solid line illustrates the optimal total fit. The gray shaded area illustrates the fitting windows and the green shaded area illustrates the wavelength range used for the iron flux calculation. In the zoom-in lower panel, the dashed lines denote the detailed components in the rest frame, including the power-law continuum, the Fe II template, the broad H $\beta$  component, the narrow H $\beta$  component, [O III]  $\lambda$ 5007, and [O III]  $\lambda$ 4959. In this case, the He II line is too weak to be displayed, so it is not shown here.

shifted with three free-fitting parameters. We typically use the default initial values for DASpec because the fitting method is insensitive to the first guess. Additionally, we impose certain constraints on the parameter ranges:  $-4 < \alpha < 2$ ,  $100 \text{ km s}^{-1} < \text{FWHM}_{\text{Fe,conv}} < 12000 \text{ km s}^{-1}$ ,  $-2500 \text{ km s}^{-1} < \text{Shift}_{\text{EL}} < 2500 \text{ km s}^{-1}$ ,  $1200 \text{ km s}^{-1} < \text{FWHM}_{\text{BEL}} < 12000 \text{ km s}^{-1}$ ,  $1 \text{ km s}^{-1} < \text{FWHM}_{\text{NEL}} < 1200 \text{ km s}^{-1}$ , where  $\alpha$  is the slope of the power-law continuum,  $\text{FWHM}_{\text{Fe,conv}}$  represents the FWHM of the convolved Gaussian profile for the Fe II template, “EL” denotes every emission line, “BEL” denotes broad emission lines, and “NEL” denotes narrow emission lines. We did not consider host galaxy components here. We will discuss the effect of host galaxies in Section 4.1. In addition, the choice of the fitting components, the Fe II templates, and the fitting windows all have influence on the fitting results. We will discuss these issues in Section 4.1. We intend to incorporate these effects as additional sources of uncertainty in our analyses.

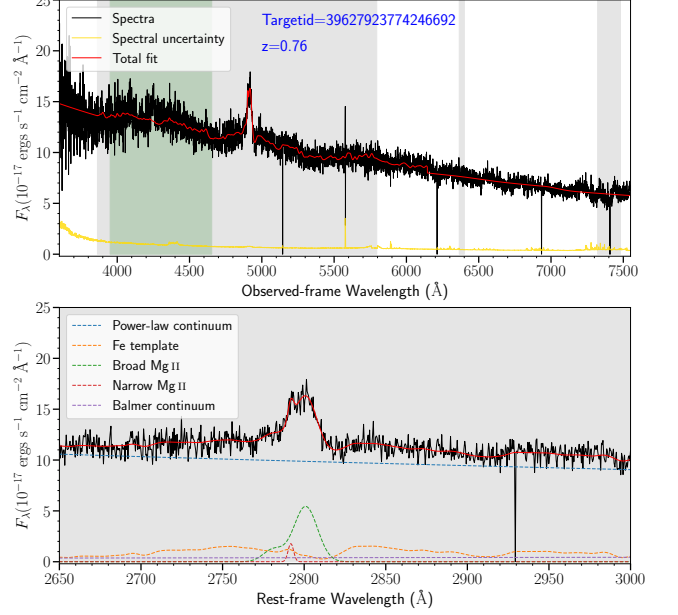


**Figure 2.** A fitting with strong iron strength in the rest-frame UV region. In the upper panel, the black solid line represents the rest-frame spectrum following correction for galactic extinction, and the yellow solid line represents the spectral uncertainty. The red solid line illustrates the optimal total fit. The gray shaded area illustrates the fitting windows and the green shaded area illustrates the wavelength range used for the iron flux calculation. In the zoom-in lower panel, the dashed lines denote the detailed components in the rest frame, including the power-law continuum, the Fe II template, the broad Mg II component, the narrow Mg II component, and the Balmer continuum.

### 3. RESULTS

In this section, we begin with the process of constructing a quasar sample with H $\beta$  (hereafter the H $\beta$  sample). We make the iron correction for H $\beta$ -based SMBH masses and perform an exploratory analysis. We then create a quasar sample with Mg II (hereafter the Mg II sample) and a quasar sample with both H $\beta$  and Mg II (hereafter the H $\beta$ -Mg II sample). Utilizing the H $\beta$ -Mg II sample, we employ the iron-corrected, H $\beta$ -based SMBH mass  $M_{\text{H}\beta,\text{corr}}$  to calibrate the iron-uncorrected Mg II-based SMBH mass  $M_{\text{Mg II,uncorr}}$ , i.e., we derive the iron-corrected  $R-L$  relation for Mg II. Here “corr” refers to iron-corrected measurements and “uncorr” refers to iron-uncorrected measurements.

#### 3.1. Iron-corrected, H $\beta$ -based SMBH Masses

To explore various single-epoch spectral characteristics associated with H $\beta$ , we have compiled fundamental parameters from the spectral fitting. These include:

- FWHM and equivalent width (EW) of the broad H $\beta$  line ( $\text{FWHM}_{\text{H}\beta}$  and  $\text{EW}_{\text{H}\beta}$ ) calculated from the best fit of the double-gaussian model. The DESI spectral resolution is high, so the instrumental broadening effect is negligible.

- Flux ratio between Fe II and H $\beta$ , denoted as

$$R_{\text{Fe,H}\beta} = F_{\text{Fe}}/F_{\text{H}\beta}, \quad (2)$$

where  $F_{\text{H}\beta}$  represents the flux of the broad H $\beta$  component, and  $F_{\text{Fe}}$  represents the flux of Fe II spanning from 4434 Å to 4684 Å.

- FWHM of Fe II, which can be expressed as

$$\text{FWHM}_{\text{Fe}} = \sqrt{\text{FWHM}_{\text{IZw1}}^2 + \text{FWHM}_{\text{Fe,conv}}^2}, \quad (3)$$

where the intrinsic FWHM of iron template  $\text{FWHM}_{\text{IZw1}}$  is constant at 900 km s $^{-1}$  (Vestergaard & Wilkes 2001).

- EW of [O III]  $\lambda$ 5007 ( $\text{EW}_{[\text{O III}]}$ ).

- Slope of the power-law continuum ( $\alpha$ ).

Given the large size of the parent sample, we are able to select quasars with good spectral quality and model fits. Finally, we established a well-defined H $\beta$  sample with 10,202 quasars using the following criteria:

$$\left\{ \begin{array}{l} \text{EW}_{\text{H}\beta,\text{error}}/\text{EW}_{\text{H}\beta} < 30\% \\ R_{\text{Fe,H}\beta,\text{error}}/R_{\text{Fe,H}\beta} < 30\% \\ \text{FWHM}_{\text{H}\beta,\text{error}}/\text{FWHM}_{\text{H}\beta} < 30\% \\ \text{EW}_{[\text{O III}],\text{error}}/\text{EW}_{[\text{O III}]} < 30\% \\ \text{FWHM}_{\text{H}\beta} > 1500 \text{ km s}^{-1} \\ \chi^2 < 1.3 \\ \alpha < 0, \end{array} \right. \quad (4)$$

where the reduced  $\chi^2$  reflects the fitting performance, and “error” denotes the  $1\sigma$  uncertainty of the measurements. We simulated 100 spectra for each object, considering the uncertainties associated with all components. The standard deviation of the simulated results for each parameter is treated as the uncertainty.

While most of these selection criteria are geared towards a high S/N, we also impose constraints on  $\alpha$  (see Figure 3 in Pan et al. 2022) and  $\text{FWHM}_{\text{H}\beta}$  (see Section 6.2 in Netzer 2013) to focus on blue quasars with typical broad lines, which minimizes contamination from host galaxies. Figure 3 illustrates the parameter distributions of the parent sample and H $\beta$  sample. They are broadly consistent, while the H $\beta$  sample has more robust measurements. For example, the median relative

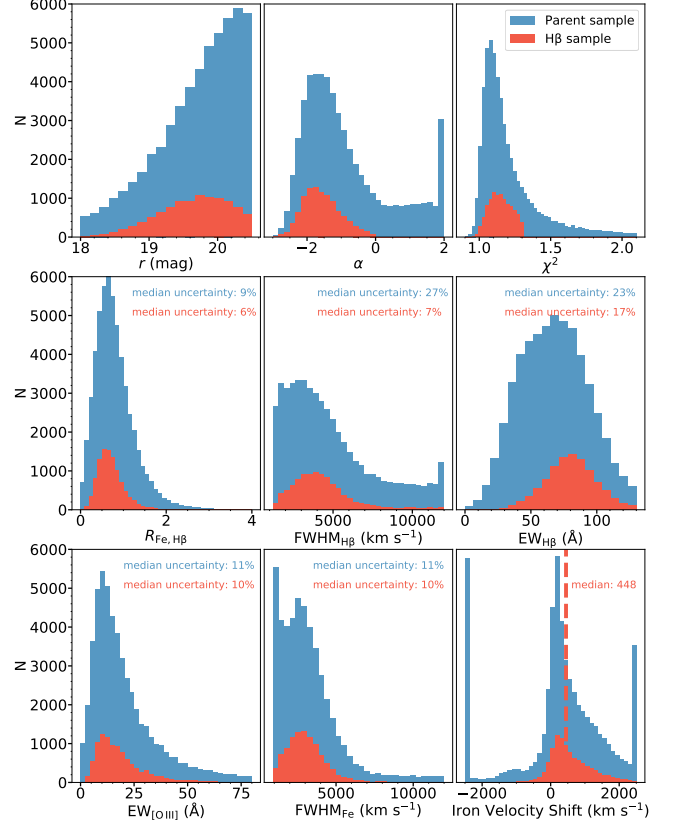


**Figure 3.** Parameter distributions of the parent sample and the H $\beta$  sample, color-coded with blue and orange. The nine panels display the  $r$  magnitude, slope of the power-law continuum,  $\chi^2$ , flux ratio between Fe II and H $\beta$ , FWHM of broad H $\beta$ , EW of broad H $\beta$ , EW of [O III]  $\lambda$ 5007, FWHM of Fe II, and velocity shift of Fe II, respectively. Five panels display the median uncertainty associated with each parameter, indicating that the H $\beta$  sample has more robust measurements than the parent sample.

error of  $\text{FWHM}_{\text{H}\beta}$  in the H $\beta$  sample is approximately 7%, and the median relative error of  $L_{5100}$  is around 1%. The last panel of Figure 3 reveals that a significant portion of quasars exhibit redshifted Fe II emission, with a median velocity of 448 km s $^{-1}$ , which is consistent with previous results (e.g., Hu et al. 2008).

In this work, we adopt  $\log(R_{\text{H}\beta}/\text{ltd}) = 1.53 + 0.51 \log l_{44}$  as the canonical H $\beta$ -based  $R$ - $L$  relation (Du et al. 2018), where ltd is the light day and  $l_{44} = L_{5100}/(10^{44} \text{ erg s}^{-1})$ . This relation is derived from quasars with low Eddington ratios, and it is almost identical to the relation of Bentz et al. (2013).

We also investigate other latest  $R$ - $L$  relations. For example, Woo et al. (2024) included more AGNs with moderate to high luminosities and discovered an  $R$ - $L$  relation with a shallower slope of  $\sim 0.4$ . Later, Wang & Woo (2024) combined this sample with existing samples

from the literature to conduct a uniform RM analysis. In the upper panel of Figure 4, we present the distribution of  $R_{\text{BLR}}$  and  $L_{5100}$  from the best average sample in Wang & Woo (2024). The super-Eddington sample, shown in red, is clearly located below the  $R$ - $L$  relation established by Bentz et al. (2013) and Du et al. (2018). It is important to note that the super-Eddington sample is predominantly composed of high-luminosity AGNs, which can explain the shallower slope of  $R_{\text{BLR}}$  versus  $L_{5100}$  by Wang & Woo (2024). The lower panel of Figure 4 more clearly illustrates the correlation between the  $R_{\text{BLR}}$  departure and the Eddington ratio. Wang & Woo (2024) also confirmed that sub-Eddington and super-Eddington AGNs exhibit systematic offsets in the  $R$ - $L$  relation. These results support that a correction for the Eddington ratio, as indicated by the iron strength, is necessary.

We adopt the iron-calibrated  $R$ - $L$  relation from Du & Wang (2019) to estimate the  $\text{H}\beta$ -based SMBH mass  $M_{\text{H}\beta}$  with the form of

$$\log(R_{\text{H}\beta}/\text{ltcd}) = 1.65 + 0.45 \log l_{44} - 0.35 R_{\text{Fe,H}\beta}, \quad (5)$$

where the definition of  $R_{\text{Fe,H}\beta}$  is consistent with Du & Wang (2019). Then Equation 1 can be employed to derive the iron-uncorrected and iron-corrected,  $\text{H}\beta$ -based SMBH masses,  $M_{\text{H}\beta,\text{uncorr}}$  and  $M_{\text{H}\beta,\text{corr}}$ . We assume that the  $f$ -factor is 1.1. Its substantial uncertainty will be discussed in Section 4.1. The value of 1.1 is converted from the zero point of Equation 1 in Vestergaard & Osmer (2009) for consistency. This is also consistent with Woo et al. (2015). We will show that the choice of 1.1 provides a fair comparison between  $\text{H}\beta$ -based and  $\text{Mg II}$ -based SMBH masses. Then we measure the bolometric luminosity  $L_{\text{Bol}}$ . Considering that the bolometric correction factor  $k_{\text{Bol}}$  is dependent on various parameters such as accretion rate and SMBH mass (Jin et al. 2012), we adopt Equation 3 from Netzer (2019), i.e.,  $k_{\text{Bol}} = 40 \times l_{42}^{-0.2}$ , where  $l_{42} = L_{5100}/(10^{42} \text{ erg s}^{-1})$ . We admit an average uncertainty of 0.2 dex for the bolometric correction (Netzer 2019), but this has little impact on the following analysis. Figure 5 shows the typical ranges of the bolometric luminosities and SMBH masses in the  $\text{H}\beta$  sample. The marginal positive correlation between  $M_{\text{H}\beta}$  and  $L_{5100}$  is reasonable, as more massive quasars are generally more luminous. Additionally, we compute the Eddington ratio ( $L_{\text{Bol}}/L_{\text{Edd}}$ ), where  $L_{\text{Edd}} = 1.5 \times 10^{38} (M_{\text{SMBH}}/M_{\odot})$  denotes the Eddington luminosity for gas with solar composition.

Figure 6 highlights the correlations between the Eddington ratio and  $R_{\text{Fe,H}\beta}$ . In our DESI sample, a notable positive correlation with the rms scatter of 0.38 dex is observed, affirming that the  $R_{\text{Fe,H}\beta}$  term can serve as

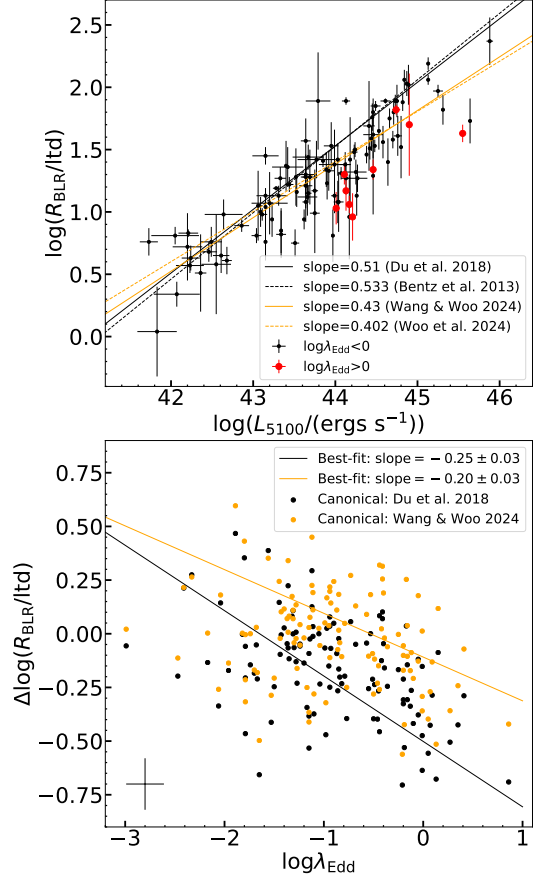


**Figure 4.** Upper: distribution of  $R_{\text{BLR}}$  and  $L_{5100}$  from the best average sample in Wang & Woo (2024). The black and red dots represent the sub-Eddington and super-Eddington sample, respectively. The lines illustrate four  $R$ - $L$  relations for comparison. Lower: correlation between  $R_{\text{BLR}}$  departure and the Eddington ratio. The black and orange colors represent the  $R_{\text{BLR}}$  departure relative to the canonical  $R$ - $L$  relation from Du et al. (2018) and Wang & Woo (2024), respectively. The solid lines indicate the best-fit results from the linear regression. The black cross indicates the typical statistical error bar. Our findings confirm that sub-Eddington and super-Eddington AGNs exhibit systematic offsets in the  $R$ - $L$  relation, highlighting the necessity for the iron correction.

a reliable tracer of the Eddington ratio. When we divide the sample into groups with different masses, the marginal correlations persist. It is important to note that the corrected  $M_{\text{SMBH}}$  is dependent on  $R_{\text{Fe,H}\beta}$  according to the formula itself, which enhances the correlation.

Correlations between corrected and uncorrected  $M_{\text{H}\beta}$  and  $L_{\text{Bol}}/L_{\text{Edd}}$  are depicted in Figure 7. The upper panels compare the distributions of the Eddington ratios and SMBH masses before and after the correction. Following the correction, we estimate that the fraction of super-Eddington quasars is around 5%, significantly

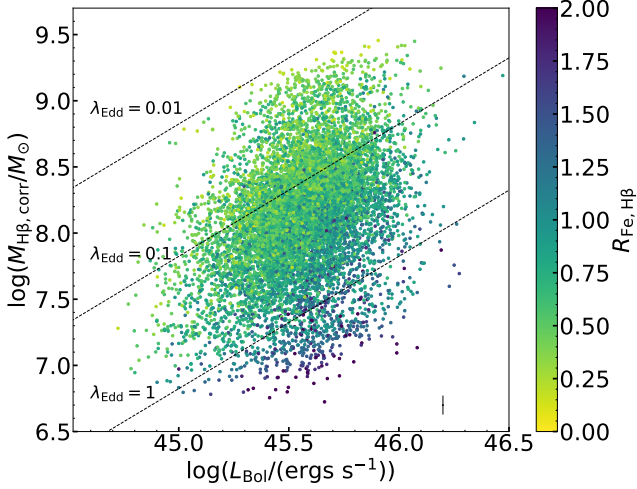


**Figure 5.** The distribution of bolometric luminosity and black hole masses in the H $\beta$  sample, color-coded by  $R_{\text{Fe,H}\beta}$ . The black cross indicates the typical statistical error bar. The dashed lines show the constant Eddington ratios of 0.01, 0.1, and 1, respectively. A reasonable marginal positive correlation is observed between  $M_{\text{H}\beta}$  and  $L_{\text{Bol}}$ . Additionally, at fixed  $M_{\text{H}\beta}$ ,  $L_{\text{Bol}}$  increases with larger  $R_{\text{Fe,H}\beta}$ , suggesting a relationship between  $R_{\text{Fe}}$  and the Eddington ratio.

higher than the uncorrected value of 0.4%. The lower panels of Figure 7 show that the masses of most quasars are overestimated by up to 0.7 dex, and the mass correction factor shows an anticorrelation with the Eddington ratio. The mean correction is about 0.16 dex (equivalent to a factor of 1.5), and the rms and standard deviation are around 0.19 and 0.11 dex, respectively. Although the mean correction of 0.16 dex is comparable to or smaller than the typical uncertainty of single-epoch SMBH masses, this correction represents a systematic offset driven by the Eddington ratio, and thus is meaningful and necessary.

In Figure 8, the relationships between  $\text{FWHM}_{\text{Fe}}$ ,  $\text{FWHM}_{\text{H}\beta}$ , and the Eddington ratio are displayed. The widths of H $\beta$  are consistently larger than those of Fe II. This pattern was previously found in the SDSS quasar sample, as discussed in Hu et al. (2008). Their findings indicate that  $\text{FWHM}_{\text{Fe}} = \frac{3}{4} \text{FWHM}_{\text{H}\beta}$ , proposing an association between the optical Fe II emission and the so-called intermediate-width H $\beta$  component that originates from an exterior inflowing region to the BLR region. Furthermore, the relationship between the Eddington ratio and the widths in Figure 8 is consistent with previous findings, indicating that highly-accreting AGNs typically exhibit relatively narrow H $\beta$  lines.

The relation between  $R_{\text{Fe}}$  and  $\text{FWHM}_{\text{H}\beta}$  or  $\text{EW}_{[\text{O III}]}$  represents the prominent correlation of Eigenvector 1 (See Marziani et al. 2018 for a review), as shown in Figure 9. In the upper panel, coded by the Eddington

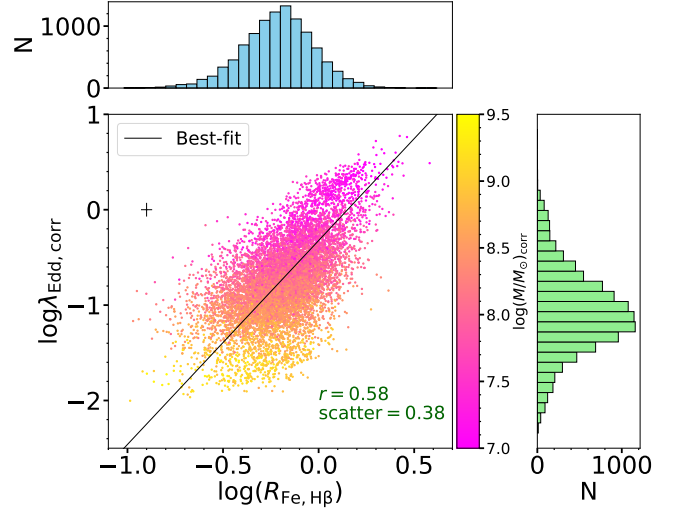


**Figure 6.** Distributions of the Eddington ratio and  $R_{\text{Fe}}$ , color-coded by  $M_{\text{H}\beta,\text{corr}}$ . The black cross indicates the typical statistical error bar.  $r$  is the Pearson correlation coefficient. The black solid line indicates the best-fit result of the linear regression. The rms scatter for the best-fit relationship is about 0.38 dex.

The notable positive correlation in our DESI sample affirms that the  $R_{\text{Fe,H}\beta}$  term can serve as a reliable tracer for the Eddington ratio.

ratio, there is a marginal anti-correlation between  $R_{\text{Fe}}$  and  $\text{FWHM}_{\text{H}\beta}$ . Such a triangle distribution of our DESI sample is consistent with previous results (e.g., Wu & Shen 2022). In the low-width regime, the influence of the Eddington ratio on the iron strength becomes more apparent in the horizontal direction. Regarding the vertical direction, the velocity dispersion is commonly attributed to the orientation effect (Marziani et al. 2001; Shen & Ho 2014). The lower panel is plotted for comparison with Figure 1 from Shen & Ho (2014), which used more than 20,000 SDSS quasars within the redshift range of  $0.1 < z < 0.9$  and the luminosity range of  $L_{5100} \approx 10^{44-45.5} \text{ erg s}^{-1}$ . Our results from DESI quasars are well consistent with the SDSS findings, revealing a clear anti-correlation between  $\text{EW}_{[\text{O III}]}$  and  $R_{\text{Fe}}$ .

### 3.2. Iron-corrected, Mg II-based SMBH Masses

As we did for the H $\beta$  sample, we compile fundamental parameters from the spectral fitting of Mg II. These include:

- FWHM and EW of broad Mg II ( $\text{FWHM}_{\text{Mg II}}$  and  $\text{EW}_{\text{Mg II}}$ ) calculated from the best fit of the double-gaussian model.
- Flux ratio between Fe II and Mg II, denoted as

$$R_{\text{Fe,Mg II}} = F_{\text{Fe}}/F_{\text{Mg II}}, \quad (6)$$



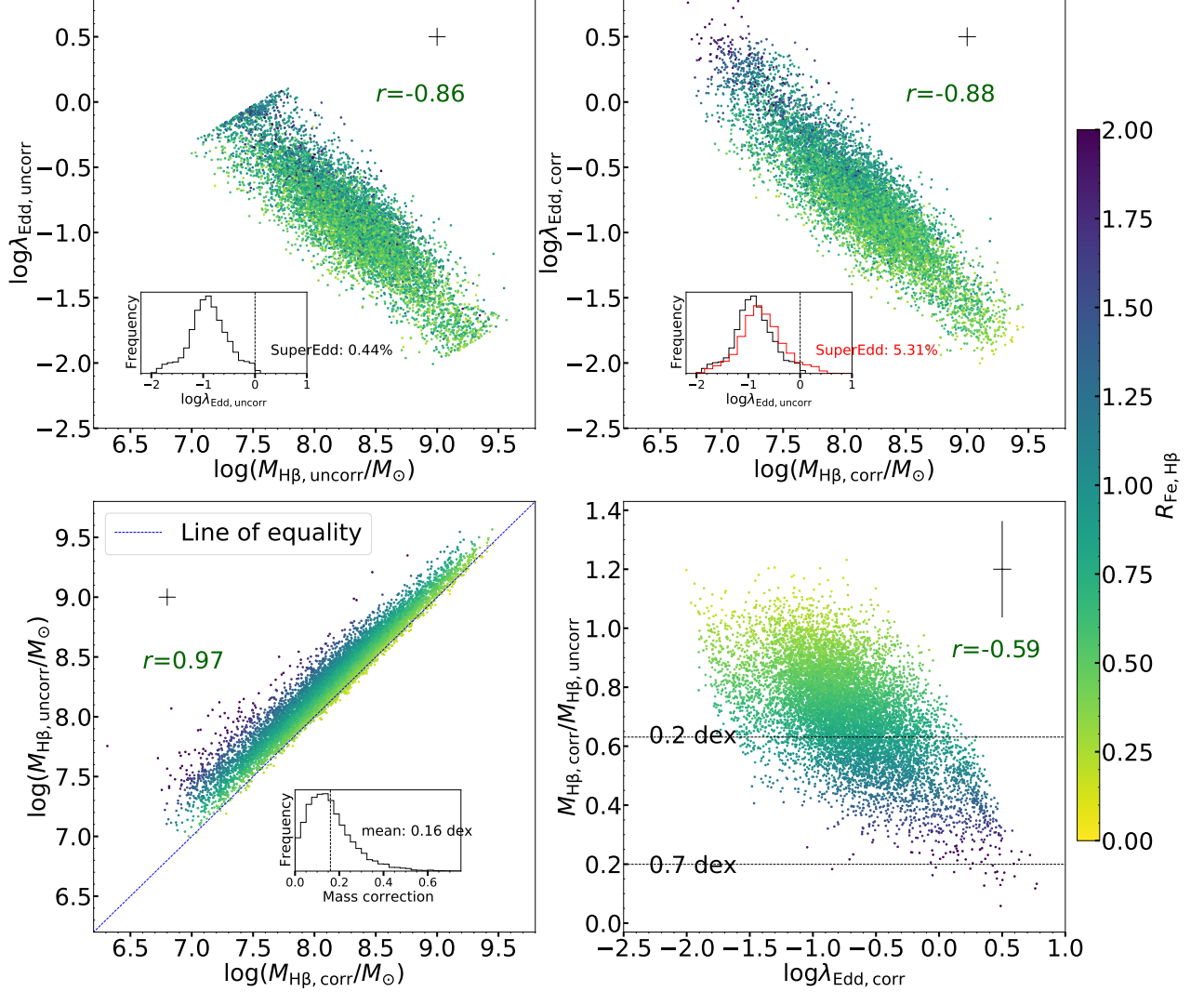


**Figure 7.** Correlations between corrected and uncorrected  $M_{H\beta}$  and Eddington ratio, color-coded by  $R_{Fe, H\beta}$ . The black cross indicates the typical statistical error bar.  $r$  is the Pearson correlation coefficient. The blue dashed line shows the line of equality. The upper inset plots show Eddington ratio distributions before and after the correction in black and red, respectively. The dashed vertical line indicated the Eddington ratio of 1. After the correction we estimate that the fraction of super-Eddington quasars is about 5%, which is significantly higher than the uncorrected value of 0.44%. The lower panels indicate that the masses of most quasars are overestimated by up to 0.7 dex, depending on the iron strength. The mean correction is about 0.16 dex (equivalent to a factor of 1.5), and the rms and standard deviation are around 0.19 and 0.11 dex, respectively.

where  $F_{Mg II}$  represents the flux of broad Mg II, and  $F_{Fe}$  represents the flux of Fe II spanning from 2250 Å to 2650 Å.

- FWHM of Fe II.
- Slope of the power-law continuum ( $\alpha$ ).

Following the procedure for the H $\beta$  sample, we generate a well-defined sample with 2335 quasars (hereafter

the Mg II sample) using the following criteria:

$$\left\{ \begin{array}{l} 0.65 < z < 0.8 \\ EW_{Mg II, error} / EW_{Mg II} < 30\% \\ R_{Fe, Mg II, error} / R_{Fe, Mg II} < 30\% \\ FWHM_{Mg II, error} / FWHM_{Mg II} < 30\% \\ FWHM_{Mg II} > 1500 \text{ km s}^{-1} \\ \chi^2 < 1.3 \\ \alpha < 0. \end{array} \right. \quad (7)$$

Figure 10 illustrates the parameter distributions for both the parent sample and the Mg II sample. The Mg II

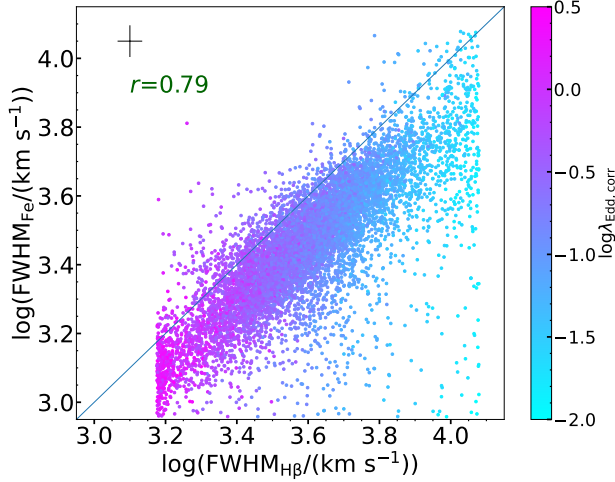


**Figure 8.** The distribution of  $\text{FWHM}_{\text{Fe}}$  and  $\text{FWHM}_{\text{H}\beta}$ , color-coded by the Eddington ratio. The black cross indicates the typical statistical error bar.  $r$  is the Pearson correlation coefficient. The blue dashed line shows the line of equality. This figure confirms that  $\text{FWHM}_{\text{Fe}} \sim \frac{3}{4} \text{FWHM}_{\text{H}\beta}$ , proposing an association between the optical Fe II emission and the so-called intermediate-width H $\beta$  component.

sample allows more robust measurements than the parent sample. The median relative error of  $\text{FWHM}_{\text{Mg II}}$  is about 7%, and the median relative error of  $L_{3000}$  is about 1%.

Then we perform a crossmatch between the H $\beta$  sample and the Mg II sample, resulting in a H $\beta$ -Mg II sample of 954 quasars. We leverage this H $\beta$ -Mg II sample to explore the relationship between H $\beta$  and Mg II. Specifically, the H $\beta$ -Mg II sample serves as the foundation to calibrate the Mg II-based SMBH mass using the estimated iron-corrected, H $\beta$ -based SMBH mass.

We illustrate the comparisons of  $L_{5100}$  versus  $L_{3000}$ ,  $\text{FWHM}_{\text{Mg II}}$  versus  $\text{FWHM}_{\text{H}\beta}$ , and  $R_{\text{Fe, H}\beta}$  versus  $R_{\text{Fe, Mg II}}$  in Figure 11. In particular, the slope of the best fit for  $\text{FWHM}_{\text{Mg II}}$  versus  $\text{FWHM}_{\text{H}\beta}$  is around 0.83. The sub-linear relation has also been identified in previous studies (e.g., Woo et al. 2018; Le et al. 2020; Rakshit et al. 2021). Conversely, some studies have found the roughly linear relation (e.g., Zuo et al. 2015). The results vary depending on different samples, fitting procedures, and templates used. We assume that the slope is roughly one and the relation between Mg II and H $\beta$  is roughly linear. Furthermore, as shown in the lower panels of Figure 11, both measurements of Fe II strength trace the Eddington ratio of quasars. The correlation between the Eddington ratio and  $R_{\text{Fe, Mg II}}$  is only slightly weaker than the correlation shown in Figure 6 (The rms scatter is 0.51 dex, compared to 0.38 dex). Therefore,

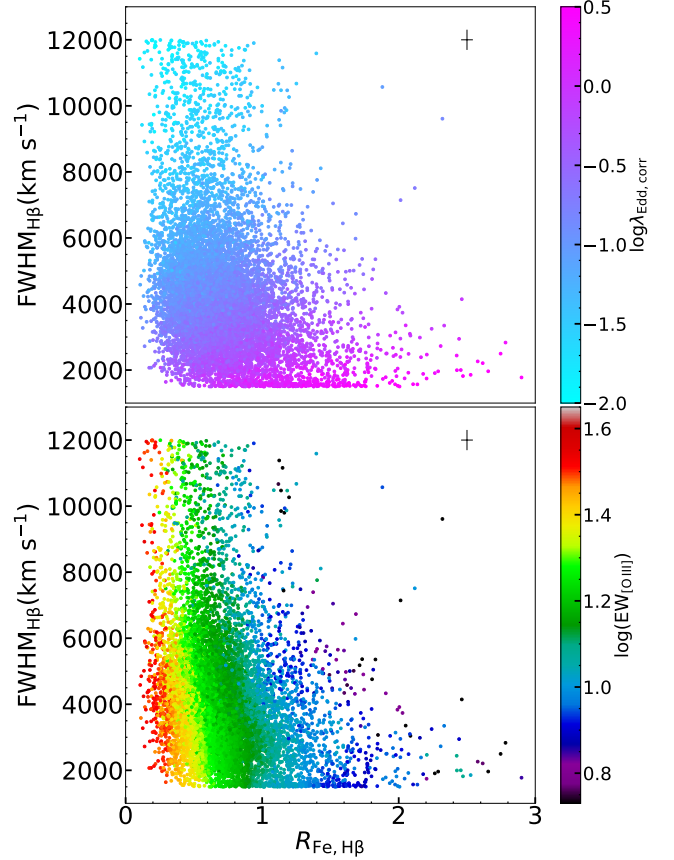


**Figure 9.** Distributions of quasar populations in the EV1 plane. The black cross indicates the typical statistical error bar. In the upper panel, the colors represent the Eddington ratio. In the lower panel, we color-code the points by  $\text{EW}_{[\text{O III}]}$ , averaged over all nearby objects in a smoothing box of  $\Delta R_{\text{Fe}} = 0.2$  and  $\Delta \text{FWHM}_{\text{H}\beta} = 1000 \text{ km s}^{-1}$ . There is an obvious systematic trend of decreasing  $\text{EW}_{[\text{O III}]}$  with increasing  $R_{\text{Fe}}$ .

we incorporate  $R_{\text{Fe, Mg II}}$  to extend the  $R$ - $L$  relation for Mg II.

The uncorrected virial mass based on Mg II  $M_{\text{Mg II, uncorr}}$  is determined using the following equation (Vestergaard & Osmer 2009, hereafter VO09):

$$M = 10^{6.86} \left( \frac{\text{FWHM}_{\text{Mg II}}}{10^3 \text{ km s}^{-1}} \right)^2 \left( \frac{L_{3000}}{10^{44} \text{ erg s}^{-1}} \right)^{0.5} M_{\odot}, \quad (8)$$

where  $L_{3000}$  is the monochromatic luminosity ( $\lambda L_{\lambda}$ ) at 3000 Å. The upper left panel of Figure 12 shows a comparison between the  $M_{\text{Mg II, uncorr}}$  and  $M_{\text{H}\beta, \text{uncorr}}$ . These two tracers are consistent with each other. The mean offset is less than 0.003 dex, which proves that the choice of the virial factor  $f$  of 1.1 in Equation 1 is appropriate. In the upper right panel of Figure 12, especially in the high Eddington ratio regime, it is noticeable that  $M_{\text{Mg II, uncorr}}$  tends to be systematically higher than

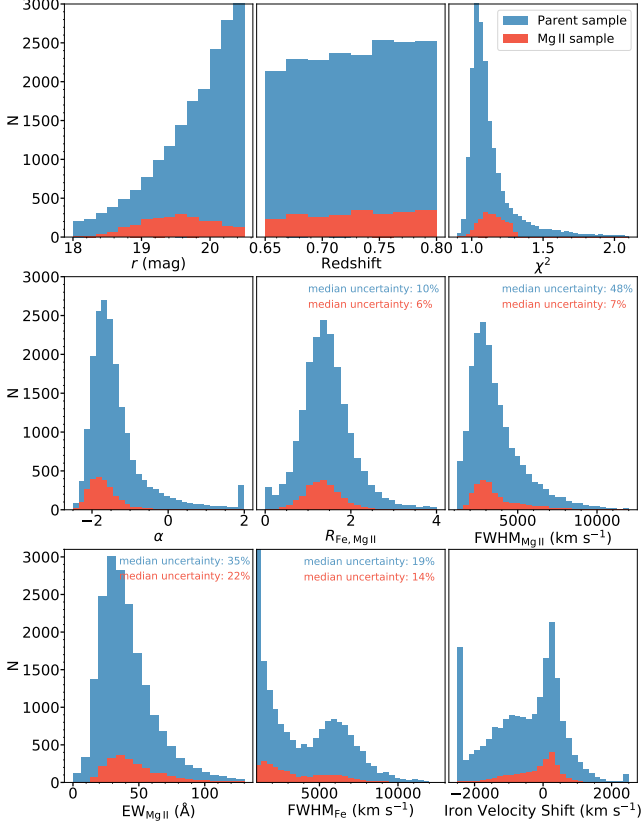


**Figure 10.** Parameter distributions of the parent sample and the Mg II sample, color-coded with blue and orange. The nine panels display the  $r$  magnitude, redshift,  $\chi^2$ , slope of the power-law continuum, flux ratio between Fe II and Mg II, FWHM of broad Mg II, EW of broad Mg II, FWHM of Fe II, and velocity shift of Fe II, respectively. Four panels display the median uncertainty associated with each parameter, indicating that the Mg II sample has more robust measurements than the parent sample.

$M_{\text{H}\beta,\text{corr}}$  due to the previously mentioned iron correction effect for  $M_{\text{H}\beta}$ .

We utilize  $M_{\text{H}\beta,\text{corr}}$  as a reference and perform a multivariable linear regression with the following form:

$$\log \frac{M_{\text{Mg II,corr}}}{M_{\odot}} = a + b \times \log \frac{\text{FWHM}_{\text{Mg II}}}{\text{km s}^{-1}} + c \times \log \frac{L_{3000}}{10^{44} \text{ erg s}^{-1}} + d \times R_{\text{Fe,Mg II}}, \quad (9)$$

where we fix  $b = 2$ . This is to compare with  $\text{H}\beta$ -based masses for consistency. This choice has been recommended and used by many previous studies (e.g., Vestergaard & Osmer 2009; Shen et al. 2011; Woo et al. 2018; Le et al. 2020; Yu et al. 2023). The best-fit results are:  $a = 1.14 \pm 0.03$ ,  $c = 0.46 \pm 0.03$ ,  $d = -0.34 \pm 0.02$ , which are very similar to the parameters of Equation 5. This similarity suggests a potential relationship between optical iron and UV iron emission. We show the

comparison between  $M_{\text{Mg II,uncorr}}$  and  $M_{\text{Mg II,corr}}$  in the lower left panel of Figure 12. The iron correction effect on  $M_{\text{Mg II}}$  is similar to that on  $M_{\text{H}\beta}$ . For the entire sample, the average correction is about a factor of 1.5, while for the super-Eddington sample, it is approximately a factor of 2.3. Finally, the lower right panel of Figure 12 demonstrates that  $M_{\text{Mg II,corr}}$  and  $M_{\text{H}\beta,\text{corr}}$  show a good overall consistency. The average offset between these two estimators is 0.03 dex, with a scatter of 0.24 dex. We observe a mean offset of 0.3 dex in the lowest mass range and 0.2 dex in the highest mass range. This discrepancy arises from the sub-linear relationship between  $\text{FWHM}_{\text{Mg II}}$  and  $\text{FWHM}_{\text{H}\beta}$ . Specifically,  $\text{FWHM}_{\text{Mg II}}$  tends to be slightly larger than  $\text{FWHM}_{\text{H}\beta}$  when the lines are very narrow, while it is typically larger than  $\text{FWHM}_{\text{H}\beta}$  when the lines are broad. Le et al. (2020) discussed this effect and suggested an additional correction term based on the profile of Mg II. In our analysis, we subtracted the narrow component of Mg II, which is a different approach from that used by Le et al. (2020). This approach makes the above discrepancy more prominent. Nonetheless, the two iron-corrected mass estimators are generally consistent within the typical total uncertainty of 0.31 dex. We again emphasize the importance of calibrating  $M_{\text{Mg II}}$  based on the accretion state, as indicated by the iron strength mentioned above.

### 3.3. SMBH Mass Estimation of DESI Quasars at $0.6 < z < 1.6$

With the iron-corrected single-epoch SMBH mass estimator for Mg II, we measure the SMBH masses of DESI quasars at  $z < 2$ . Our plan is to integrate the  $\text{H}\beta$  and Mg II estimators to provide a reliable BH mass estimation in the future. We will collaborate with other DESI SMBH mass studies and release the results as part of the DESI DR1 value-added catalog (VAC). In this paper, we restrict the SMBH mass measurements to the redshift range of  $0.6 < z < 1.6$ , only utilizing the derived Mg II estimator.

Since DESI has not released an official quasar catalog, we first build a quasar catalog as follows. We choose a primary sample from an Iron VAC (v2.0) generated by FastSpecFit (J. Moustakas et al. in preparation)<sup>2</sup>. FastSpecFit is a stellar continuum and emission-line modeling code designed for DESI. This VAC provides continuum and emission line information crucial for SMBH mass estimation. This dataset will be pub-

<sup>2</sup> <https://fastspecfit.readthedocs.io/en/latest/iron.html>

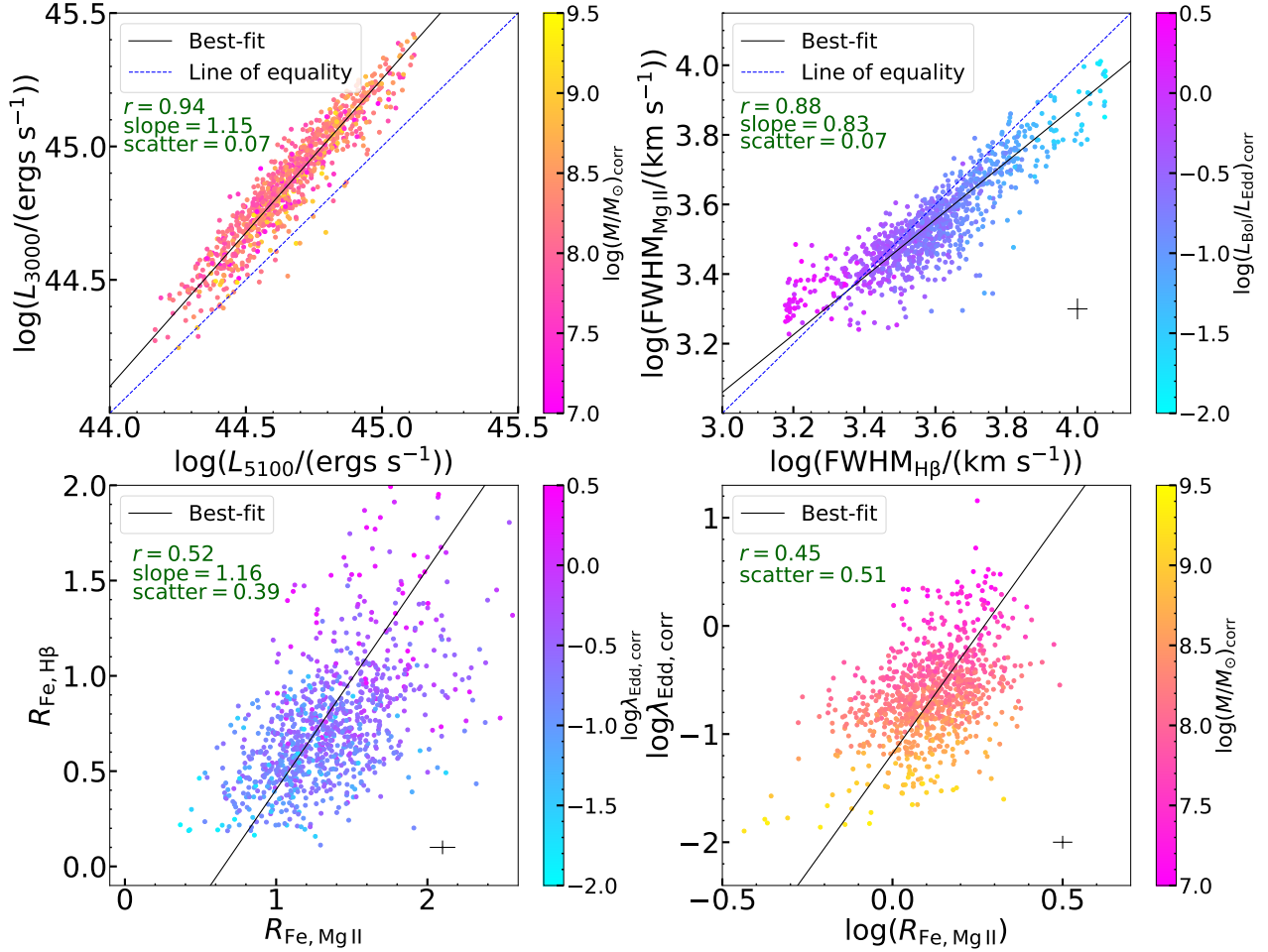


**Figure 11.** Upper left: comparison between  $L_{5100}$  and  $L_{3000}$ . Upper right: comparison between  $\text{FWHM}_{\text{Mg II}}$  and  $\text{FWHM}_{\text{H}\beta}$ , color-coded by the Eddington ratio. Lower left: comparison between  $R_{\text{Fe,H}\beta}$  and  $R_{\text{Fe,Mg II}}$ , color-coded by the Eddington ratio. Lower right: comparison between the Eddington ratio and  $R_{\text{Fe,Mg II}}$ , color-coded by  $M_{\text{H}\beta,\text{corr}}$ . The black solid line indicates the best-fit result of the linear regression. The blue dashed line shows the line of equality. The black cross indicates the typical statistical error bar.  $r$  is the Pearson correlation coefficient. The slope and rms scatter of the best fit are shown as text in the plot. The slopes of best fit for luminosity, FWHM, and iron strength are all around one, indicating a roughly linear correlation between Mg II and H $\beta$ . The lower panels suggest that both  $R_{\text{Fe,H}\beta}$  and  $R_{\text{Fe,Mg II}}$  can trace the Eddington ratio of quasars.

licly released as part of DESI DR1. We select the sample from the DESI main survey and apply constraints such as  $0.6 < z < 1.6$ ,  $r < 22$ , `spectype=="qso"`, and `survey=="main"`. There would be misclassified objects with large uncertainty in the catalog. By adding constraints to the uncertainties, users could remove them. In the future we will update our SMBH mass catalog after the release of the official DESI quasar catalog.

We apply the same fitting procedure mentioned above and utilize Equation 9 to estimate  $M_{\text{Mg II,corr}}$  with proper error propagation. Finally, we analyze 490,648 quasars listed in Table 1. Among them, approximately 35% quasars have a mass error smaller than 0.5 dex. Additionally, we estimate  $M_{\text{Mg II}}$  using the fitting results from the FastSpecFit VAC and Equation 8. In order to provide users with the convenience of choosing their pre-

ferred estimation methods, we also provide masses based on the formula derived by Shen et al. (2011, hereafter Shen11), Le et al. (2020, hereafter Le20), and Yu et al. (2023, hereafter Yu23). We will discuss the details and make the comparisons between different SMBH mass estimators in Section 4.2.

## 4. DISCUSSION

### 4.1. Uncertainties of the SMBH Masses

The SMBH mass measurements derived above depend on the fitting procedure. Hence, a key question is to test the robustness of the result. We discuss the uncertainties in this subsection.

Spectral fitting windows can influence the fitting results. We have chosen a broad window spanning 3750 to 5500 Å for the optical region to include enough fea-



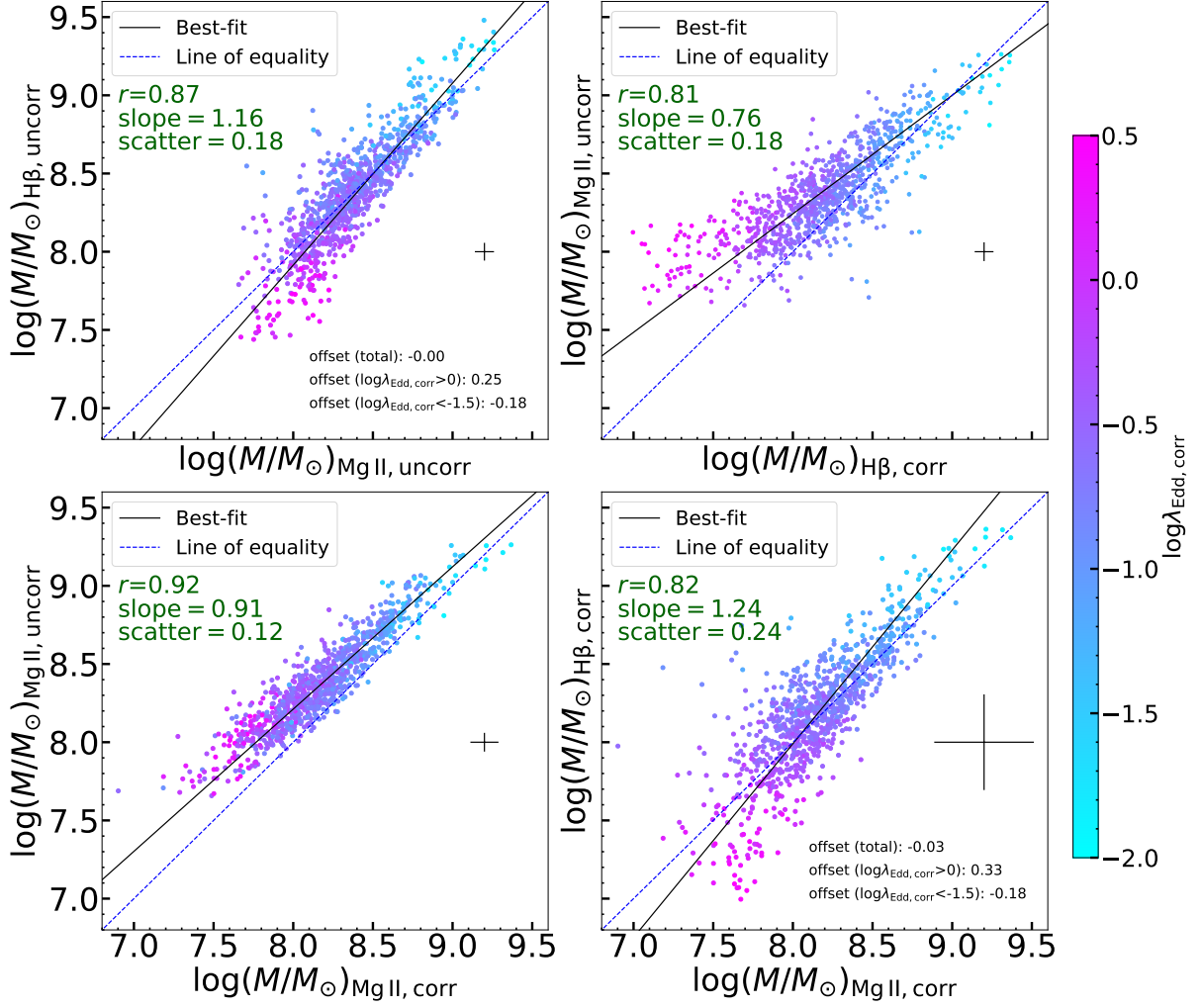


**Figure 12.** Upper left: comparison between the uncorrected  $M_{\text{Mg II}}$  and uncorrected  $M_{\text{H}\beta}$ . Upper right: comparison between uncorrected  $M_{\text{Mg II}}$  and corrected  $M_{\text{H}\beta}$ . Lower left: comparison between the uncorrected  $M_{\text{Mg II}}$  and corrected  $M_{\text{Mg II}}$ . Lower right: comparison between the uncorrected  $M_{\text{Mg II}}$  and corrected  $M_{\text{H}\beta}$ . The black solid line indicates the best-fit result of the linear regression, and the grey shaded region indicates its  $1\sigma$  uncertainty. The black crosses in the first three panels indicate the typical statistical error bar. In the lower right panel, we show the typical total uncertainty, including the statistical error and an additional 0.3 dex uncertainty from the  $f$  factor.  $r$  is the Pearson correlation coefficient. The blue dashed line shows the line of equality. The iron correction effect on  $M_{\text{Mg II}}$  is similar to that on  $M_{\text{H}\beta}$ . For the entire sample, the average correction is about a factor of 1.5, while for the super-Eddington sample, it is approximately a factor of 2.3.

tures. Compared to the windows used in Du & Wang (2019), we have added a window of 3750–4000 Å to better decompose the continuum and Fe II. Therefore, the choice of optical window is not expected to introduce a significant uncertainty. However, in the UV region, the fitting windows has some impact on the results. This sensitivity arises because part of the Fe II line lies beneath the Mg II line, making the relative flux ratio more sensitive. Another issue is related to the UV Fe II itself. While this study uses a single velocity shift parameter to regulate the iron template (consistent with most studies), individual UV iron lines may have different shifts (Vestergaard & Wilkes 2001). Consequently,

different fitting windows may be dominated by different iron lines, which introduces additional uncertainties. Furthermore, for most quasars in the H $\beta$ -Mg II sample, the Mg II line is located at the edge of spectra that have poorer S/N ratios on the blue side of Mg II. This effect leads to a weak constraint on the continuum. To estimate the additional uncertainty in a simple way, we randomly select 100 quasars from the H $\beta$ -Mg II sample. For each quasar, we fit three times with three setups of UV fitting windows, the 2200–3500 Å, 2200–3400 Å, and 2200–3600 Å windows. We do not test changing the left limit because it has already almost reached the edge of spectral coverage. For simplicity, we do not change the

**Table 1.** Fits Catalog Format

Column	Format	Units	Description
RA	float64	degree	Right Ascension
DEC	float64	degree	Declination
TARGETID	int64		Target ID
PROGRAM	string		Program ID
HEALPIX	int64		HEALPix ID
REDSHIFT	float64		Redshift from FSF
RMAG	float64	mag	$22.5 - 2.5 \log_{10}(\text{FLUX}_R)$
L3000_DAS	float64	$1 \times 10^{44}$ erg/s	Luminosity at 3000Å (DAS)
L3000_DAS_ERR	float64	$1 \times 10^{44}$ erg/s	Error of L3000_DAS
EW_DAS	float64	Å	Equivalent Width of Mg II Emission Line (DAS)
EW_DAS_ERR	float64	Å	Error of EW_DAS
FWHM_DAS	float64	km/s	Full Width at Half Maximum of Mg II Emission Line (DAS)
FWHM_DAS_ERR	float64	km/s	Error of FWHM_DAS
RFE_DAS	float64		Strength of Iron Emission in UV (DAS)
RFE_DAS_ERR	float64		Error of RFE_DAS
LOGMASS_DAS_Pan25	float64	$M_{\odot}$	Iron-corrected SMBH Mass based on Pan25 (DAS)
LOGMASS_DAS_Pan25_ERR	float64	...	Error of LOGMASS_DAS_Pan25
LOGMASS_DAS_VO09	float64	...	SMBH Mass based on VO09 (DAS)
LOGMASS_DAS_VO09_ERR	float64	...	Error of LOGMASS_DAS_VO09
LOGMASS_DAS_Shen11	float64	...	SMBH Mass based on Shen11 (DAS)
LOGMASS_DAS_Shen11_ERR	float64	...	Error of LOGMASS_DAS_Shen11
LOGMASS_DAS_Le20	float64	...	SMBH Mass based on Le20 (DAS)
LOGMASS_DAS_Le20_ERR	float64	...	Error of LOGMASS_DAS_Le20
LOGMASS_DAS_Yu23	float64	...	SMBH Mass based on Yu23 (DAS)
LOGMASS_DAS_Yu23_ERR	float64	...	Error of LOGMASS_DAS_Yu23
L3000_FSF	float64	$1 \times 10^{44}$ erg/s	Luminosity at 3000Å (FSF)
FWHM_FSF	float64	km/s	Full Width at Half Maximum of MgII Emission Line (FSF)
LOGMASS_FSF_VO09	float64	$M_{\odot}$	SMBH Mass based on VO09 (FSF)

NOTE—This table is available in its entirety in the machine-readable format. “FSF” indicates the spectral measurements obtained from FastSpecFit, while “DAS” signifies the results derived from DASpec in this paper.

fitting windows of 3625–3645 Å and 4170–4260 Å. We acknowledge that what we estimate is a lower limit of the additional uncertainty. Finally, we consider the standard deviation of 100 objects as the uncertainty. Overall, we estimate that  $\text{FWHM}_{\text{Mg II}}$ ,  $L_{3000}$ , and  $R_{\text{Fe, Mg II}}$  have additional uncertainties of 5%, 2%, and 6%, respectively.

The Mg II feature is sensitive to the Fe II emission that extends beneath the emission line. Previous studies have highlighted that the choice of the UV Fe II template can introduce significant biases to the results (e.g., Kurk et al. 2007; Woo et al. 2018; Shin et al. 2019; Yu et al. 2021). One frequently used UV iron template is from Vestergaard & Wilkes (2001, referred to as the VW01 template). The T06 template has also been widely used

(e.g., Sameshima et al. 2017; Woo et al. 2018; Shin et al. 2019). The main differences lie in their behaviors around the Mg II line (see Figure 1 in Lai et al. 2024). The T06 template incorporates the Fe II contribution beneath the Mg II line, employing a model spectrum based on a photoionization calculation of the BLR clouds. In contrast, the VW01 template lacks Fe II flux in this region, leading to an overestimation of the actual Mg II flux. However, determining the optimal template remains challenging. Lai et al. (2024) considered four empirical and semi-empirical UV iron templates: VW01 template, T06 template, the template from Bruhweiler & Verner (2008), and the template from Mejía-Restrepo et al. (2016). They derived the final line properties and measurement uncertainties from the mean results ob-

tained using these four different iron templates. Following the same methodology, we fit the 100 quasars with four setups of the iron templates mentioned above. We estimate that there is a systematic difference of about 29% between the mean  $R_{\text{Fe,MgII}}$  based on four templates. It is risky to define such a systematic difference as an uncertainty because we do not know the true value. Since the mean  $R_{\text{Fe,MgII}}$  based on the T06 template has an intermediate result, we adopt the T06 template for this work. Besides, the influence of templates on  $\text{FWHM}_{\text{MgII}}$  and  $L_{300}$  is about 4%. Therefore, we acknowledge that the lower limit of the additional uncertainty caused by iron templates is about 4%.

The choice of fitting components for emission lines can slightly affect the results. Our study utilized a line model comprising one narrow Gaussian component and two broad Gaussian components for  $\text{H}\beta$ . In contrast, some studies use one narrow and three broad Gaussian components to characterize  $\text{H}\beta$  (e.g., Rakshit et al. 2020; Yang et al. 2023). Given our primary focus on flux ratios, the impact of the number of  $\text{H}\beta$  components is minimal. Regarding  $[\text{O III}]$ , previous works sometimes use one Gaussian for the narrow component (the “core” component) and a second Gaussian profile for the potentially broadened and blueshifted component (the “wing” component). The velocity shift and dispersion of the narrow  $\text{H}\beta$  are tied to those of the  $[\text{O III}]$  “core” component. However, it is challenging to distinguish the two components robustly. More important, for most objects, the “core” component dominates the whole  $[\text{O III}]$ . Therefore, we use one Gaussian to characterize  $[\text{O III}]$ . Similarly, we choose two, not three, broad Gaussian components for  $\text{Mg II}$ . We have also explored the necessity of including Balmer continuum emission. We observed a significant degeneracy between the Balmer and power-law continuum when the fitting windows of the UV region are narrow. Considering this, we adopt the current broad fitting windows to better constrain the Balmer continuum. In summary, our choice of emission line components is reasonable and is expected to introduce negligible uncertainties.

We also test the influence of the host galaxy. Based on a spectrophotometric decomposition technique introduced by Sun et al. (in preparation), we randomly fit 1000 quasars at  $z \sim 0.6$  from Table 1. The results suggest that the host galaxy fraction anticorrelates with the quasar luminosity. In the range of  $10^{45} \text{ erg s}^{-1} < L_{\text{Bol}} < 10^{46} \text{ erg s}^{-1}$ , the average optical host fraction is about 20% and the UV host fraction is about 5%, which is consistent with recent results (e.g. Shen et al. 2011; Jalan et al. 2023). In addition, Jalan et al. (2023) found anticorrelations between the host galaxy fraction and

iron strength, Eddington ratio, and redshift. Therefore, for the majority of objects in our  $\text{H}\beta$ - $\text{Mg II}$  sample at  $0.65 < z < 0.8$ , host galaxy contamination should have little effect on the final results.

In order to incorporate the above effects, we add an additional uncertainty of 10% for FWHM and  $R_{\text{Fe}}$ . The typical final uncertainties of the two parameters are 0.055 dex and 0.052 dex, respectively. We apply a correction of 20% for  $L_{5100}$  to exclude the host galaxy contribution. This introduces an additional uncertainty 25% and leads to a typical final uncertainty of 0.109 dex. Similarly, we apply a correction of 5% to  $L_{3000}$ , and its typical final uncertainty is 0.044 dex. Following the same procedure as introduced in Section 3.2, we obtain the best fit of  $d = -0.29 \pm 0.02$  when we fix the parameter  $c = 0.46$ . The value of  $-0.29$  is roughly consistent with  $-0.34$  within a  $2 \sigma$  level, confirming the need for the iron correction.

In the context of a specified line width, the virial f-factor is contingent on the geometry and kinematics of the BLR gas, exhibiting significant variations across different objects. The virial f-factor can range from approximately 0.5 (Graham et al. 2011) to 1.1 (Woo et al. 2013). Its determination often involves comparing the virialized SMBH masses to the expected SMBH masses derived from the local  $M$ - $\sigma$  relation. Note that different works use different velocity indicators, such as  $\sigma$  or FWHM. Additionally, the  $M$ - $\sigma$  relation is dependent on galaxy bulge properties, suggesting that different virial coefficients should be applied based on the bulge classification of the host galaxy, with values around 1.1 for classical bulges and 0.6 for pseudobulges (Ho & Kim 2014). However, choosing the most appropriate f-factor based on different types is challenging, leading to intrinsic scatter in the f-factor. Consequently, a mean value is often employed for SMBH mass estimations. Our study assumed a mean f-factor of 1.1, converted from Vestergaard & Osmer (2009). We acknowledge an intrinsic scatter of approximately 0.3 dex (Shen et al. 2024), constituting a major source of uncertainty in single-epoch SMBH mass estimations. It is essential to note that, since our focus is on the systematic iron correction of the  $\text{Mg II}$ -based SMBH mass, the absolute f-factor of  $\text{H}\beta$  estimators only affects the absolute mass measurements but not the calibration formula.

Altogether, we estimate that the overall systematic uncertainty of a single-epoch SMBH mass is approximately 0.4-0.5 dex, significantly larger than the typical measurement error. The primary purpose of this work is to reduce the systematic offset rather than the scatter of mass estimations by introducing the iron correction.

The derived iron-corrected  $R$ - $L$  relation for Mg II is robust.

#### 4.2. Comparison with Previous Mg II-based SMBH Mass Estimators

The differences of SMBH mass estimators can be attributed to numerous factors, such as sample construction, fitting procedures, the  $f$ -factor, the form of the formula, and more. In this subsection, we delve into the complexities by determining masses using various estimators and drawing comparisons to investigate the systematic differences.

As listed in Table 1, we have selected four estimators from the literature for comparison. These estimators have parameters as follows.

$$\begin{aligned}
 \text{VO09} : (a, b, c, d) &= (0.86, 2, 0.5, 0) \\
 \text{Shen11} : (a, b, c, d) &= (0.74, 2, 0.62, 0) \\
 \text{Le20} : (a, b, c, d) &= (1.04, 2, 0.5, 0) \\
 \text{Yu23} : (a, b, c, d) &= (1.01, 2, 0.39, 0) \\
 \text{Pan25} : (a, b, c, d) &= (1.14, 2, 0.46, -0.34).
 \end{aligned} \tag{10}$$

We estimate the Mg II-based masses based on these formulas and display the mass distributions and median masses of different estimators in Figure 13. VO09 (purple) serves as a reference estimator, while Pan25 (red) indicates the measurements using Equation 9 in this work. Overall, the average iron correction is about 0.2 dex.

Shen11 (blue) allowed the luminosity index  $c$  to vary, yet they employed the same calibration as VO09, resulting in a negligible systematic offset between the outcomes of VO09 and Shen11. Le20 (green) utilized a sample with a large luminosity range to calibrate the best-fit parameters of the Mg II estimator. Their best-fit model fixed  $b = 2$  and  $c = 0.5$  with a large fitted value of  $a$ , which is consistent with the results reported by Woo et al. (2018). Thus, the median mass of Le20 is systematically larger by around 0.2 dex than that of Shen11, which has been reported and discussed in Le et al. (2020). Shen11 subtracted the narrow component of Mg II and derived systematically higher  $\text{FWHM}_{\text{Mg II}}$ , which led to a smaller calibration result of  $a$  for a given fiducial mass compared to Le20. Yu23 (yellow) used their latest RM results and derived  $c = 0.39$ , which is shallower than the canonical value of 0.5. This estimator obtains slightly larger median BH mass than VO09 due to the different calibration and best-fit parameters. The black dashed line is the result from VO09 with FastSpecFit fitting results, which did not consider the Fe II template. This led to an overestimation of the continuum

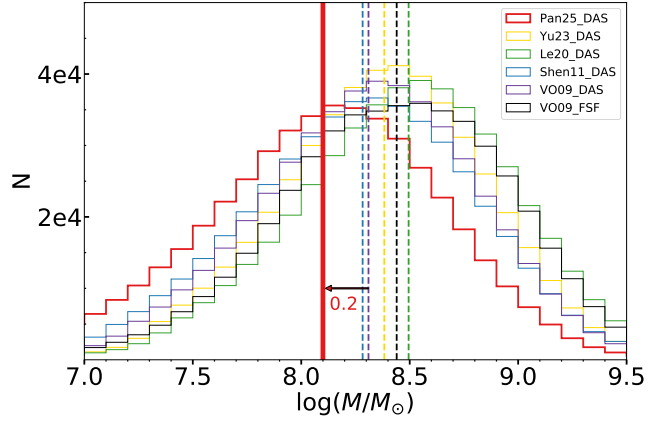


**Figure 13.** Mg II-based SMBH mass distributions of different estimators. The red solid line represents the median mass estimated by Equation 9 in this paper (Pan25), which is the only iron-corrected estimator among them. The black dashed line represents the median mass estimated by VO09 with the fitting results from the FastSpecFit. The remaining colors denote the estimators VO09, Shen11, Le20, and Yu23 with the fitting results derived by this paper. The average mass reduction caused by the iron correction is about 0.2 dex.

luminosity and  $\text{FWHM}_{\text{Mg II}}$ , and thus an overestimation of SMBH masses.

Due to the systematic discrepancies caused by various factors (e.g., iron correction, virial factor  $f$ , components of Mg II, fixed or free parameters, and Fe II templates), caution should be taken when selecting SMBH mass estimators. Therefore, we provide the original  $\text{FWHM}$  and luminosity values in Table 1, and users can easily use their preferred mass estimators. In the future, more and more RM and interferometric results will help to better study the effect of the iron correction and to derive a better estimator.

#### 4.3. Implications

We further investigate whether the iron correction is also valid at higher redshifts, particularly in the range of  $z > 6$  when the universe is less than one billion years old. Recent observations of quasars at high redshift are difficult to reconcile with black hole formation and growth scenarios because they require extremely massive seeds and rapidly accrete gas at the Eddington or even super-Eddington rate (see Inayoshi et al. 2020 for a review). For example, SDSS J010013.02+280225.8 is an extremely massive quasar at  $z = 6.3$  with an estimated SMBH mass of  $1.2 \times 10^{10} M_{\odot}$  (Wu et al. 2015). Wang et al. (2018) reported a quasar at  $z = 7.0$  with a mass of approximately  $1.3 \times 10^9 M_{\odot}$ . The James Webb Space Telescope (JWST) also observed a quasar at  $z = 7.1$  with a mass of about  $1.5 \times 10^9 M_{\odot}$  (Bosman et al.



2023) and an AGN at  $z = 8.5$  with a mass of about  $1.5 \times 10^8 M_{\odot}$  (Kokorev et al. 2023). Besides, many JWST programs including ASPIRE (e.g., Yang et al. 2023; Wang & Aspire Team 2024), CEERS (e.g., Finkelstein et al. 2023; Larson et al. 2023), and UNCOVER (e.g., Bezanson et al. 2022; Goulding et al. 2023), have revealed a large population of AGNs in the early universe. The ongoing JWST observations will continue to identify a larger population of massive quasars, suggesting different scenarios for the assembly of SMBHs.

Most of these high-redshift luminous quasars host billion solar-mass black holes and have high Eddington ratios (e.g., Yang et al. 2023; Larson et al. 2023; Goulding et al. 2023), it is natural to ask whether this population requires the iron correction mentioned above. If the iron-corrected  $R-L$  relations for  $H\beta$  and  $Mg\text{II}$  are confirmed in the early universe, it suggests that current measurements of high-redshift SMBH masses are significantly overestimated by around 0.4 dex on average. To some extent, the tension of the required massive seeds could be relieved by such a mass reduction. Therefore, we plan to collect a high-redshift sample and study its properties to address this question in the future.

## 5. SUMMARY

In this study, we assembled a parent sample of more than 55,000 type 1 quasars in the redshift range of  $0.25 < z < 0.8$  from a DESI internal data release. We used versatile spectral fitting techniques to measure the spectral properties of the quasars, including continuum and line emission in the UV and optical ranges. We then estimated SMBH masses of the quasars and corrected the mass measurements using the iron emission line strength.

Our best  $H\beta$  sample consists of more than 10,000 quasars. We calculated their SMBH masses using the iron-corrected  $R-L$  relation that accounts for the accretion state, which caused a mass reduction of up to 0.7 dex. Our analysis revealed that approximately 5% of super-Eddington quasars exist in this sample, showcasing a notable positive correlation and affirming the reliability of the  $R_{\text{Fe},H\beta}$  term as a tracer for the Eddington ratio. We also confirmed a relation between the  $\text{FWHM}_{\text{Fe}}$  and  $\text{FWHM}_{H\beta}$  emissions that suggests a connection between the optical Fe II emission and the intermediate-width  $H\beta$  component. Our findings agree closely with the previous SDSS results, highlighting a clear anti-correlation between  $\text{EW}_{[\text{O III}]}$  and  $R_{\text{Fe}}$ .

Furthermore, we constructed a  $H\beta$ - $Mg\text{II}$  sample comprising around 1000 type 1 quasars at  $0.65 < z < 0.8$ . Using the iron-corrected,  $H\beta$ -based SMBH mass, we calibrated  $Mg\text{II}$ -based SMBH masses and established the

iron-corrected  $R-L$  relation for  $Mg\text{II}$ . The derived relation takes the form  $\log(R_{\text{MgII}}/\text{Itd}) \sim 0.46 \log l_{44} - 0.34 R_{\text{Fe}}$ . Notably, their iron-corrected SMBH masses are approximately 0 to 0.4 dex lower than classic single-epoch SMBH masses. If this iron correction still holds in the early universe, the tension of very massive SMBH seeds could be alleviated. We also conducted comparisons between our results and those of previous estimators. In general, they are consistent, but some minor systematic differences still exist. Leveraging the derived  $Mg\text{II}$  estimator, we provided SMBH masses for around 0.5 million DESI quasars at  $0.6 < z < 1.6$ , with a plan to expand this dataset in the future.

## DATA AVAILABILITY

All the material needed to reproduce the figures of this publication is available at this site: <https://doi.org/10.5281/zenodo.14673134>.

## ACKNOWLEDGMENTS

We acknowledge support from the National Key R&D Program of China (2021YFA1600404), the National Science Foundation of China (12225301), and the China Manned Space Project (CMS-CSST-2021-A05, CMS-CSST-2021-A06). We thank DESI Internal Reviewers (Mar Mezcuca and Jinyi Yang) for very helpful discussions and comments and thank DESI PubBoard Handler (Vanina Ruhlmann-Kleider) for timely help. We thank Jian-Min Wang, Pu Du, Luis C. Ho, Yuxuan Pang, and Masafusa Onoue for very helpful discussions and comments. HZ acknowledge the supports from National Key R&D Program of China (grant Nos. 2023YFA1607800, 2022YFA1602902, 2023YFA1608100) and the National Natural Science Foundation of China (NSFC; grant Nos. 12120101003, 12373010, 12233008) and the Strategic Priority Research Program of the Chinese Academy of Science (Grant no. XDB0550100).

This material is based upon work supported by the U.S. Department of Energy (DOE), Office of Science, Office of High-Energy Physics, under Contract No. DE-AC02-05CH11231, and by the National Energy Research Scientific Computing Center, a DOE Office of Science User Facility under the same contract. Additional support for DESI was provided by the U.S. National Science Foundation (NSF), Division of Astronomical Sciences under Contract No. AST-0950945 to the NSF's National Optical-Infrared Astronomy Research Laboratory; the Science and Technology Facilities Council of the United Kingdom; the Gordon and Betty Moore Foundation; the Heising-Simons Foundation; the French Alternative Energies and Atomic Energy Commission (CEA); the National

Council of Humanities, Science and Technology of Mexico (CONAHCYT); the Ministry of Science and Innovation of Spain (MICINN), and by the DESI Member Institutions: <https://www.desi.lbl.gov/collaborating-institutions>. Any opinions, findings, and conclusions or recommendations expressed in this material are those of the author(s) and do not necessarily reflect the views of the U. S. National Science Foundation, the U. S. Department of Energy, or any of the listed funding agencies. The authors are honored to be permitted to con-

duct scientific research on Iolkam Du’ag (Kitt Peak), a mountain with particular significance to the Tohono O’odham Nation.

*Facilities:* DESI

*Software:* Astropy(Astropy Collaboration et al. 2013, 2018, 2022), Topcat(Taylor 2005), FastSpecFit(Moustakas 2023), DASpec

## REFERENCES

- Abuter, R., Allouche, F., Amorim, A., et al. 2024, *Nature*, 627, 281, doi: [10.1038/s41586-024-07053-4](https://doi.org/10.1038/s41586-024-07053-4)
- Alexander, D. M., Davis, T. M., Chaussidon, E., et al. 2023, *AJ*, 165, 124, doi: [10.3847/1538-3881/acacfc](https://doi.org/10.3847/1538-3881/acacfc)
- Astropy Collaboration, Robitaille, T. P., Tollerud, E. J., et al. 2013, *A&A*, 558, A33, doi: [10.1051/0004-6361/201322068](https://doi.org/10.1051/0004-6361/201322068)
- Astropy Collaboration, Price-Whelan, A. M., Sipőcz, B. M., et al. 2018, *AJ*, 156, 123, doi: [10.3847/1538-3881/aabc4f](https://doi.org/10.3847/1538-3881/aabc4f)
- Astropy Collaboration, Price-Whelan, A. M., Lim, P. L., et al. 2022, *ApJ*, 935, 167, doi: [10.3847/1538-4357/ac7c74](https://doi.org/10.3847/1538-4357/ac7c74)
- Bentz, M. C., Peterson, B. M., Pogge, R. W., Vestergaard, M., & Onken, C. A. 2006, *ApJ*, 644, 133, doi: [10.1086/503537](https://doi.org/10.1086/503537)
- Bentz, M. C., Denney, K. D., Grier, C. J., et al. 2013, *ApJ*, 767, 149, doi: [10.1088/0004-637X/767/2/149](https://doi.org/10.1088/0004-637X/767/2/149)
- Bezanson, R., Labbe, I., Whitaker, K. E., et al. 2022, arXiv e-prints, arXiv:2212.04026, doi: [10.48550/arXiv.2212.04026](https://doi.org/10.48550/arXiv.2212.04026)
- Boroson, T. A., & Green, R. F. 1992, *ApJS*, 80, 109, doi: [10.1086/191661](https://doi.org/10.1086/191661)
- Bosman, S. E. I., Álvarez-Márquez, J., Colina, L., et al. 2023, arXiv e-prints, arXiv:2307.14414, doi: [10.48550/arXiv.2307.14414](https://doi.org/10.48550/arXiv.2307.14414)
- Bruhweiler, F., & Verner, E. 2008, *ApJ*, 675, 83, doi: [10.1086/525557](https://doi.org/10.1086/525557)
- Busca, N., & Bolland, C. 2018, arXiv e-prints, arXiv:1808.09955, doi: [10.48550/arXiv.1808.09955](https://doi.org/10.48550/arXiv.1808.09955)
- Cackett, E. M., Bentz, M. C., & Kara, E. 2021, *iScience*, 24, 102557, doi: [10.1016/j.isci.2021.102557](https://doi.org/10.1016/j.isci.2021.102557)
- Chaussidon, E., Yèche, C., Palanque-Delabrouille, N., et al. 2023, *ApJ*, 944, 107, doi: [10.3847/1538-4357/acb3c2](https://doi.org/10.3847/1538-4357/acb3c2)
- Cho, H., Woo, J.-H., Wang, S., et al. 2023, *ApJ*, 953, 142, doi: [10.3847/1538-4357/ace1e5](https://doi.org/10.3847/1538-4357/ace1e5)
- Coatman, L., Hewett, P. C., Banerji, M., et al. 2017, *MNRAS*, 465, 2120, doi: [10.1093/mnras/stw2797](https://doi.org/10.1093/mnras/stw2797)
- DESI Collaboration, Aghamousa, A., Aguilar, J., et al. 2016a, arXiv e-prints, arXiv:1611.00036, doi: [10.48550/arXiv.1611.00036](https://doi.org/10.48550/arXiv.1611.00036)
- . 2016b, arXiv e-prints, arXiv:1611.00037, doi: [10.48550/arXiv.1611.00037](https://doi.org/10.48550/arXiv.1611.00037)
- DESI Collaboration, Abareshi, B., Aguilar, J., et al. 2022, *AJ*, 164, 207, doi: [10.3847/1538-3881/ac882b](https://doi.org/10.3847/1538-3881/ac882b)
- DESI Collaboration, Adame, A. G., Aguilar, J., et al. 2024a, arXiv e-prints, arXiv:2404.03000, doi: [10.48550/arXiv.2404.03000](https://doi.org/10.48550/arXiv.2404.03000)
- . 2024b, arXiv e-prints, arXiv:2404.03001, doi: [10.48550/arXiv.2404.03001](https://doi.org/10.48550/arXiv.2404.03001)
- . 2024c, arXiv e-prints, arXiv:2404.03002, doi: [10.48550/arXiv.2404.03002](https://doi.org/10.48550/arXiv.2404.03002)
- DESI Collaboration, Adame, A. G., Aguilar, J., et al. 2024d, *AJ*, 167, 62, doi: [10.3847/1538-3881/ad0b08](https://doi.org/10.3847/1538-3881/ad0b08)
- . 2024e, *AJ*, 168, 58, doi: [10.3847/1538-3881/ad3217](https://doi.org/10.3847/1538-3881/ad3217)
- Dey, A., Schlegel, D. J., Lang, D., et al. 2019, *AJ*, 157, 168, doi: [10.3847/1538-3881/ab089d](https://doi.org/10.3847/1538-3881/ab089d)
- Dong, X.-B., Wang, J.-G., Ho, L. C., et al. 2011, *ApJ*, 736, 86, doi: [10.1088/0004-637X/736/2/86](https://doi.org/10.1088/0004-637X/736/2/86)
- Du, P., & Wang, J.-M. 2019, *ApJ*, 886, 42, doi: [10.3847/1538-4357/ab4908](https://doi.org/10.3847/1538-4357/ab4908)
- Du, P., Hu, C., Lu, K.-X., et al. 2015, *ApJ*, 806, 22, doi: [10.1088/0004-637X/806/1/22](https://doi.org/10.1088/0004-637X/806/1/22)
- Du, P., Zhang, Z.-X., Wang, K., et al. 2018, *ApJ*, 856, 6, doi: [10.3847/1538-4357/aaae6b](https://doi.org/10.3847/1538-4357/aaae6b)
- Fan, X., Bañados, E., & Simcoe, R. A. 2023, *ARA&A*, 61, 373, doi: [10.1146/annurev-astro-052920-102455](https://doi.org/10.1146/annurev-astro-052920-102455)
- Farr, J., Font-Ribera, A., & Pontzen, A. 2020, *JCAP*, 2020, 015, doi: [10.1088/1475-7516/2020/11/015](https://doi.org/10.1088/1475-7516/2020/11/015)
- Finkelstein, S. L., Leung, G. C. K., Bagley, M. B., et al. 2023, arXiv e-prints, arXiv:2311.04279, doi: [10.48550/arXiv.2311.04279](https://doi.org/10.48550/arXiv.2311.04279)
- Fitzpatrick, E. L. 1999, *PASP*, 111, 63, doi: [10.1086/316293](https://doi.org/10.1086/316293)
- Goulding, A. D., Greene, J. E., Setton, D. J., et al. 2023, *ApJL*, 955, L24, doi: [10.3847/2041-8213/acf7c5](https://doi.org/10.3847/2041-8213/acf7c5)

- Graham, A. W., Onken, C. A., Athanassoula, E., & Combes, F. 2011, *MNRAS*, 412, 2211, doi: [10.1111/j.1365-2966.2010.18045.x](https://doi.org/10.1111/j.1365-2966.2010.18045.x)
- GRAVITY Collaboration, Amorim, A., Bourdarot, G., et al. 2024, arXiv e-prints, arXiv:2401.07676, doi: [10.48550/arXiv.2401.07676](https://doi.org/10.48550/arXiv.2401.07676)
- Greene, J. E., & Ho, L. C. 2005, *ApJ*, 630, 122, doi: [10.1086/431897](https://doi.org/10.1086/431897)
- Grier, C. J., Trump, J. R., Shen, Y., et al. 2017, *ApJ*, 851, 21, doi: [10.3847/1538-4357/aa98dc](https://doi.org/10.3847/1538-4357/aa98dc)
- Guy, J., Bailey, S., Kremin, A., et al. 2023, *AJ*, 165, 144, doi: [10.3847/1538-3881/acb212](https://doi.org/10.3847/1538-3881/acb212)
- Ho, L. C., & Kim, M. 2014, *ApJ*, 789, 17, doi: [10.1088/0004-637X/789/1/17](https://doi.org/10.1088/0004-637X/789/1/17)
- Hormann, J. K., Martini, P., Davis, T. M., et al. 2019, *MNRAS*, 487, 3650, doi: [10.1093/mnras/stz1539](https://doi.org/10.1093/mnras/stz1539)
- Hu, C., Wang, J.-M., Ho, L. C., et al. 2008, *ApJ*, 687, 78, doi: [10.1086/591838](https://doi.org/10.1086/591838)
- Inayoshi, K., Visbal, E., & Haiman, Z. 2020, *ARA&A*, 58, 27, doi: [10.1146/annurev-astro-120419-014455](https://doi.org/10.1146/annurev-astro-120419-014455)
- Jalan, P., Rakshit, S., Woo, J.-J., Kotilainen, J., & Stalin, C. S. 2023, *MNRAS*, 521, L11, doi: [10.1093/mnras/slad014](https://doi.org/10.1093/mnras/slad014)
- Jin, C., Ward, M., & Done, C. 2012, *MNRAS*, 425, 907, doi: [10.1111/j.1365-2966.2012.21272.x](https://doi.org/10.1111/j.1365-2966.2012.21272.x)
- Kaspi, S., Brandt, W. N., Maoz, D., et al. 2007, *ApJ*, 659, 997, doi: [10.1086/512094](https://doi.org/10.1086/512094)
- Kaspi, S., Smith, P. S., Netzer, H., et al. 2000, *ApJ*, 533, 631, doi: [10.1086/308704](https://doi.org/10.1086/308704)
- Kelly, B. C., & Shen, Y. 2013, *ApJ*, 764, 45, doi: [10.1088/0004-637X/764/1/45](https://doi.org/10.1088/0004-637X/764/1/45)
- Khadka, N., Zajaček, M., Panda, S., Martínez-Aldama, M. L., & Ratra, B. 2022, *MNRAS*, 515, 3729, doi: [10.1093/mnras/stac1940](https://doi.org/10.1093/mnras/stac1940)
- Kokorev, V., Fujimoto, S., Labbe, I., et al. 2023, *ApJL*, 957, L7, doi: [10.3847/2041-8213/ad037a](https://doi.org/10.3847/2041-8213/ad037a)
- Kurk, J. D., Walter, F., Fan, X., et al. 2007, *ApJ*, 669, 32, doi: [10.1086/521596](https://doi.org/10.1086/521596)
- Lai, S., Onken, C. A., Wolf, C., Bian, F., & Fan, X. 2024, *MNRAS*, 527, 3912, doi: [10.1093/mnras/stad3474](https://doi.org/10.1093/mnras/stad3474)
- Lan, T.-W., Tojeiro, R., Armengaud, E., et al. 2023, *ApJ*, 943, 68, doi: [10.3847/1538-4357/aca5fa](https://doi.org/10.3847/1538-4357/aca5fa)
- Larson, R. L., Finkelstein, S. L., Kocevski, D. D., et al. 2023, *ApJL*, 953, L29, doi: [10.3847/2041-8213/ace619](https://doi.org/10.3847/2041-8213/ace619)
- Le, H. A. N., Woo, J.-H., & Xue, Y. 2020, *ApJ*, 901, 35, doi: [10.3847/1538-4357/abada0](https://doi.org/10.3847/1538-4357/abada0)
- Li, W., Inayoshi, K., Onoue, M., & Toyouchi, D. 2023, *ApJ*, 950, 85, doi: [10.3847/1538-4357/acbbbe](https://doi.org/10.3847/1538-4357/acbbbe)
- Lira, P., Kaspi, S., Netzer, H., et al. 2018, *ApJ*, 865, 56, doi: [10.3847/1538-4357/aada45](https://doi.org/10.3847/1538-4357/aada45)
- Ma, Q., Wu, X.-B., Gu, H., Wen, Y., & Fu, Y. 2023, *ApJ*, 949, 22, doi: [10.3847/1538-4357/acc4c1](https://doi.org/10.3847/1538-4357/acc4c1)
- Martínez-Aldama, M. L., Zajaček, M., Czerny, B., & Panda, S. 2020, *ApJ*, 903, 86, doi: [10.3847/1538-4357/abb6f8](https://doi.org/10.3847/1538-4357/abb6f8)
- Marziani, P., Sulentic, J. W., Zwitter, T., Dultzin-Hacyan, D., & Calvani, M. 2001, *ApJ*, 558, 553, doi: [10.1086/322286](https://doi.org/10.1086/322286)
- Marziani, P., Dultzin, D., Sulentic, J. W., et al. 2018, *Frontiers in Astronomy and Space Sciences*, 5, 6, doi: [10.3389/fspas.2018.00006](https://doi.org/10.3389/fspas.2018.00006)
- McHardy, I. M., Connolly, S. D., Horne, K., et al. 2018, *MNRAS*, 480, 2881, doi: [10.1093/mnras/sty1983](https://doi.org/10.1093/mnras/sty1983)
- Mejía-Restrepo, J. E., Trakhtenbrot, B., Lira, P., Netzer, H., & Capellupo, D. M. 2016, *MNRAS*, 460, 187, doi: [10.1093/mnras/stw568](https://doi.org/10.1093/mnras/stw568)
- Metzroth, K. G., Onken, C. A., & Peterson, B. M. 2006, *ApJ*, 647, 901, doi: [10.1086/505525](https://doi.org/10.1086/505525)
- Miller, T. N., Doel, P., Gutierrez, G., et al. 2023, arXiv e-prints, arXiv:2306.06310, doi: [10.48550/arXiv.2306.06310](https://doi.org/10.48550/arXiv.2306.06310)
- Moustakas, J. 2023, *FastSpecFit: Fast spectral synthesis and emission-line fitting of DESI spectra*, *Astrophysics Source Code Library*, record ascl:2308.005. <http://ascl.net/2308.005>
- Myers, A. D., Moustakas, J., Bailey, S., et al. 2023, *AJ*, 165, 50, doi: [10.3847/1538-3881/aca5f9](https://doi.org/10.3847/1538-3881/aca5f9)
- Netzer, H. 2013, *The Physics and Evolution of Active Galactic Nuclei*
- . 2019, *MNRAS*, 488, 5185, doi: [10.1093/mnras/stz2016](https://doi.org/10.1093/mnras/stz2016)
- Osterbrock, D. E., & Ferland, G. J. 2006, *Astrophysics of gaseous nebulae and active galactic nuclei*
- Pan, Z., Jiang, L., Fan, X., Wu, J., & Yang, J. 2022, *ApJ*, 928, 172, doi: [10.3847/1538-4357/ac5aab](https://doi.org/10.3847/1538-4357/ac5aab)
- Peterson, B. M. 1993, *PASP*, 105, 247, doi: [10.1086/133140](https://doi.org/10.1086/133140)
- Peterson, B. M., & Wandel, A. 1999, *ApJL*, 521, L95, doi: [10.1086/312190](https://doi.org/10.1086/312190)
- Raichoor, A., Moustakas, J., Newman, J. A., et al. 2023, *AJ*, 165, 126, doi: [10.3847/1538-3881/acb213](https://doi.org/10.3847/1538-3881/acb213)
- Rakshit, S., Stalin, C. S., & Kotilainen, J. 2020, *ApJS*, 249, 17, doi: [10.3847/1538-4365/ab99c5](https://doi.org/10.3847/1538-4365/ab99c5)
- Rakshit, S., Stalin, C. S., Kotilainen, J., & Shin, J. 2021, *ApJS*, 253, 28, doi: [10.3847/1538-4365/abd9bb](https://doi.org/10.3847/1538-4365/abd9bb)
- Richards, G. T., Strauss, M. A., Fan, X., et al. 2006, *AJ*, 131, 2766, doi: [10.1086/503559](https://doi.org/10.1086/503559)
- Sameshima, H., Yoshii, Y., & Kawara, K. 2017, *ApJ*, 834, 203, doi: [10.3847/1538-4357/834/2/203](https://doi.org/10.3847/1538-4357/834/2/203)
- Schlafly, E. F., Kirkby, D., Schlegel, D. J., et al. 2023, *AJ*, 166, 259, doi: [10.3847/1538-3881/ad0832](https://doi.org/10.3847/1538-3881/ad0832)

- Shen, X., Hopkins, P. F., Faucher-Giguère, C.-A., et al. 2020, *MNRAS*, 495, 3252, doi: [10.1093/mnras/staa1381](https://doi.org/10.1093/mnras/staa1381)
- Shen, Y., & Ho, L. C. 2014, *Nature*, 513, 210, doi: [10.1038/nature13712](https://doi.org/10.1038/nature13712)
- Shen, Y., Richards, G. T., Strauss, M. A., et al. 2011, *ApJS*, 194, 45, doi: [10.1088/0067-0049/194/2/45](https://doi.org/10.1088/0067-0049/194/2/45)
- Shen, Y., Grier, C. J., Horne, K., et al. 2024, *ApJS*, 272, 26, doi: [10.3847/1538-4365/ad3936](https://doi.org/10.3847/1538-4365/ad3936)
- Shin, J., Nagao, T., Woo, J.-H., & Le, H. A. N. 2019, *ApJ*, 874, 22, doi: [10.3847/1538-4357/ab05da](https://doi.org/10.3847/1538-4357/ab05da)
- Silber, J. H., Fagrellius, P., Fanning, K., et al. 2023, *AJ*, 165, 9, doi: [10.3847/1538-3881/ac9ab1](https://doi.org/10.3847/1538-3881/ac9ab1)
- Taylor, M. B. 2005, in *Astronomical Society of the Pacific Conference Series*, Vol. 347, *Astronomical Data Analysis Software and Systems XIV*, ed. P. Shopbell, M. Britton, & R. Ebert, 29
- Trakhtenbrot, B., & Netzer, H. 2012, *MNRAS*, 427, 3081, doi: [10.1111/j.1365-2966.2012.22056.x](https://doi.org/10.1111/j.1365-2966.2012.22056.x)
- Tsuzuki, Y., Kawara, K., Yoshii, Y., et al. 2006, *ApJ*, 650, 57, doi: [10.1086/506376](https://doi.org/10.1086/506376)
- Vestergaard, M. 2002, *ApJ*, 571, 733, doi: [10.1086/340045](https://doi.org/10.1086/340045)
- Vestergaard, M., & Osmer, P. S. 2009, *ApJ*, 699, 800, doi: [10.1088/0004-637X/699/1/800](https://doi.org/10.1088/0004-637X/699/1/800)
- Vestergaard, M., & Wilkes, B. J. 2001, *ApJS*, 134, 1, doi: [10.1086/320357](https://doi.org/10.1086/320357)
- Wang, F., & Aspire Team. 2024, in *American Astronomical Society Meeting Abstracts*, Vol. 56, *American Astronomical Society Meeting Abstracts*, 317.08
- Wang, F., Yang, J., Fan, X., et al. 2018, *ApJL*, 869, L9, doi: [10.3847/2041-8213/aaf1d2](https://doi.org/10.3847/2041-8213/aaf1d2)
- Wang, J.-M., Du, P., Li, Y.-R., et al. 2014a, *ApJL*, 792, L13, doi: [10.1088/2041-8205/792/1/L13](https://doi.org/10.1088/2041-8205/792/1/L13)
- Wang, J.-M., Qiu, J., Du, P., & Ho, L. C. 2014b, *ApJ*, 797, 65, doi: [10.1088/0004-637X/797/1/65](https://doi.org/10.1088/0004-637X/797/1/65)
- Wang, S., & Woo, J.-H. 2024, *ApJS*, 275, 13, doi: [10.3847/1538-4365/ad74f2](https://doi.org/10.3847/1538-4365/ad74f2)
- Wang, S., Shen, Y., Jiang, L., et al. 2020, *ApJ*, 903, 51, doi: [10.3847/1538-4357/abb36d](https://doi.org/10.3847/1538-4357/abb36d)
- Warner, C., Hamann, F., & Dietrich, M. 2004, *ApJ*, 608, 136, doi: [10.1086/386325](https://doi.org/10.1086/386325)
- Wills, B. J., Netzer, H., & Wills, D. 1985, *ApJ*, 288, 94, doi: [10.1086/162767](https://doi.org/10.1086/162767)
- Woo, J.-H., Le, H. A. N., Karouzos, M., et al. 2018, *ApJ*, 859, 138, doi: [10.3847/1538-4357/aabf3e](https://doi.org/10.3847/1538-4357/aabf3e)
- Woo, J.-H., Schulze, A., Park, D., et al. 2013, *ApJ*, 772, 49, doi: [10.1088/0004-637X/772/1/49](https://doi.org/10.1088/0004-637X/772/1/49)
- Woo, J.-H., Yoon, Y., Park, S., Park, D., & Kim, S. C. 2015, *ApJ*, 801, 38, doi: [10.1088/0004-637X/801/1/38](https://doi.org/10.1088/0004-637X/801/1/38)
- Woo, J.-H., Wang, S., Rakshit, S., et al. 2024, *ApJ*, 962, 67, doi: [10.3847/1538-4357/ad132f](https://doi.org/10.3847/1538-4357/ad132f)
- Wu, J., Shen, Y., Jiang, L., et al. 2022, *MNRAS*, 517, 2659, doi: [10.1093/mnras/stac2833](https://doi.org/10.1093/mnras/stac2833)
- Wu, Q., & Shen, Y. 2022, *ApJS*, 263, 42, doi: [10.3847/1538-4365/ac9ead](https://doi.org/10.3847/1538-4365/ac9ead)
- Wu, X.-B., Wang, F., Fan, X., et al. 2015, *Nature*, 518, 512, doi: [10.1038/nature14241](https://doi.org/10.1038/nature14241)
- Yang, J., Fan, X., Gupta, A., et al. 2023, *ApJS*, 269, 27, doi: [10.3847/1538-4365/acf99b](https://doi.org/10.3847/1538-4365/acf99b)
- Yèche, C., Palanque-Delabrouille, N., Claveau, C.-A., et al. 2020, *Research Notes of the American Astronomical Society*, 4, 179, doi: [10.3847/2515-5172/abc01a](https://doi.org/10.3847/2515-5172/abc01a)
- Yu, L.-M., Zhao, B.-X., Bian, W.-H., Wang, C., & Ge, X. 2020, *MNRAS*, 491, 5881, doi: [10.1093/mnras/stz3387](https://doi.org/10.1093/mnras/stz3387)
- Yu, Z., Martini, P., Penton, A., et al. 2021, *MNRAS*, 507, 3771, doi: [10.1093/mnras/stab2244](https://doi.org/10.1093/mnras/stab2244)
- . 2023, *MNRAS*, 522, 4132, doi: [10.1093/mnras/stad1224](https://doi.org/10.1093/mnras/stad1224)
- Zhou, R., Dey, B., Newman, J. A., et al. 2023, *AJ*, 165, 58, doi: [10.3847/1538-3881/aca5fb](https://doi.org/10.3847/1538-3881/aca5fb)
- Zou, H., Zhou, X., Fan, X., et al. 2017, *PASP*, 129, 064101, doi: [10.1088/1538-3873/aa65ba](https://doi.org/10.1088/1538-3873/aa65ba)
- Zuo, W., Wu, X.-B., Fan, X., et al. 2015, *ApJ*, 799, 189, doi: [10.1088/0004-637X/799/2/189](https://doi.org/10.1088/0004-637X/799/2/189)